23/082

UCRL-JC-127102
PREPRINT

Vertical Stability Analysis of Tokamaks Using a Variational Procedure

S.W. Haney, L.D. Pearlstein, R.H. Bulmer
Lawrence Livermore National Laboratory

J.P. Freidberg
Massachusetts Institute of Technology

This paper was prepared for submittal to
Plasma Physics Reports
Michael Ioffe Special Issue #9
September 1997

March 28, 1997

Lawrence Livermore National Laboratory

April 3, 1997

Vertical Stability Analysis of Tokamaks Using a Variational Procedure

S.W. Haney L.D. Pearlstein R.H. Bulmer
Lawrence Livermore National Laboratory
P.O. Box 808
Livermore, CA 94550

J.P. Freidberg
Massachusetts Institute of Technology
167 Albany St.
Cambridge, MA 02139

A variational procedure has been developed to determine the growth rate and displacement of an arbitrarily shaped ideal magnetohydrodynamic (MHD) plasma in the presence of an arbitrary set of resistive conductors and feedback circuits. A simplified version of this formalism for calculating axisymmetric ($n = 0$) stability of single and double null tokamaks has been incorporated as a module in the TEQ free boundary equilibrium code. The speed of the calculation and the direct coupling to the equilibrium code allow for comprehensive examinations of design space. This code has been used in the design of the Tokamak Physics Experiment (TPX) and the International Thermonuclear Experimental Reactor (ITER). We discuss three of these applications: (1) an examination of vertical stability as a function of poloidal beta and normalized internal inductance, (2) a study of single null versus double null stability, and (3) an exploration of feedback system design.

I. Introduction

With sufficient elongation and no conducting wall, a finite aspect ratio plasma is ideally unstable to vertical motion with growth times on the order of shear Alfvén times. Adding enough conducting structure near the plasma can stabilize the ideal magnetohydrodynamic (MHD) modes, providing there is an effective toroidal current path. Then, the plasma is unstable with time scales on the order of the much slower L/R times of the conducting structure. A feedback system is used to control unstable motion at these much slower growth rates. Since the mode is toroidally symmetric, this feedback can be supplied by poloidal field coils. Vertical stability is an important ingredient in the design and control of modern, non-circular tokamaks. Codes capable of accurately modeling vertical plasma motion, including the effects of realistic plasma and conductor geometry, are therefore critical tools for experimentalists and designers. The usefullness of such codes is dramatically enhanced if they are also fast, robust, and versatile. In this paper, we describe the implementation of such a code.

The plasma physics community has devoted a lot of effort toward modelling vertical stability. The most accurate and comprehensive codes—the Tokamak Simulation Code (TSC),[1] CORSICA,[2,3] and DINA[4]—evolve an axisymmetric plasma in time, consistent with the nonlinear MHD equations and the circuit equations governing the passive and active conductors. These codes have been highly successful at modeling both vertical stability and vertical disruption events, but they are not always robust and are extremely time-consuming to run. Eliminating the time dependence and nonlinear MHD in favor of the linear MHD normal mode equations results in a significant savings in computational time. This is the approach employed in the Nova-W code.[5] Ideal MHD codes, such as GATO[6] and ERATO,[7] have been used to determine ideal MHD stability in the presence of an ideally conducting wall. However, they give no information about resistive growth rates or feedback requirements and do not consider realistic conductor geometries. To obtain this sort of information, many have employed simplified plasma models coupled to a more complete set of circuit equations.[8,9] For example, several codes treat the plasma as a sum of one or more current filaments that move rigidly in the presense of other filaments representing the active and passive conductors. This approach is fast, but the results can be difficult to bound.[10] On the one hand, it employs a special (rigid) trial function, which is stabilizing. On the other hand, it no longer conserves the plasma flux, thus violating a constraint, which is destabilizing.

In this paper, we describe a variational approach that incorporates a realistic plasma model and a realistic set of circuit equations. This leads to a fast and accurate modelling tool that has played an important role in the design of the Tokamak Physics Experiment (TPX) and the International Thermonuclear Experimental Reactor (ITER).[11–13]

In our work, the plasma is modelled as an axisymmetric ($n = 0$) ideal MHD fluid. The passive structure, which provides the wall stabilization, is modelled as a toroidally symmetric set of finite cross-section wires with resistance. Feedback voltage is applied to some of the wires on the basis of up/down asymmetric flux measurement detected by a pair of measuring coils, the direct motion of the magnetic axis, or "gap" measurements between the plasma surface and predefined control points. We assume that the growth rates have been greatly reduced from their ideal values by the resistive wires. In this case, the plasma kinetic energy is quite small and can be neglected. Thus the time dependence is controlled by the impedance of the electrical circuits. Neglecting plasma inertia also allows analytic elimination of two of the three components of the dispacement, leading to a variational principle that depends only upon the normal component, $X = \xi \cdot \nabla\psi$. The plasma response is evaluated by substituting a large number of trial functions into the variational principle and solving for the set that minimizes the energy while simultaneously satisfying the circuit equations describing current evolution in the wires. Although the solution to the variational equations only produces the one displacement component, in the small inertia limit, it is possible to obtain the remaining components using perturbation theory.

Treating the plasma as an MHD fluid is important for obtaining a reliable estimate of its vertical stability properties. For example, we have found that multifilament models can underestimate growth rates for strongly shaped plasmas by over a factor of two. The impact of plasma resistivity occurs on a time scale much longer than that of the instability, so the error in using ideal MHD is often small. There is two caveats. First, if the plasma is bounded by a separatrix, the plasma resistivity in the edge region might be more important. Second, surface currents generated by the ideal plasma motion would rapidly diffuse. We do not consider such effects in this paper, but remind the reader that they bear examination.

The paper is organized as follows. In Section II, we present the variational formalism. Specifically, we derive a non-self-adjoint variational principle for the full system, including feedback. Minimizing this Lagrangian generates the eigenvalue equations that we solve. In Section III, we describe the trial functions we use and consider numerical issues such as convergence. We also discuss the implementation of this procedure as a module in the TEQ free-boundary MHD equilibrium code. Next, in Section IV, we present applications. First, we discuss the variation in vertical stability as a function of poloidal beta and normalized internal inductance ℓ_i. We find that, contrary to conventional wisdom, growth rates can have a minimum at some value of ℓ_i. This result was later described by Ward, Bondeson, and Hofmann[14] after discussions with one of the authors. The increase in the growth rate at the low ℓ_i side (broad current profiles) has important implications for tokamak design. Another new result, also discussed in Section IV, is the realization that double null configurations are more unstable than single null configurations. Finally, we present examples of feedback system design studies for the ITER device. We conclude in Section V with a summary, closing comments, and suggestions for future work.

II. Variational Formulation

A. Governing Equations

We wish to model a system consisting of a plasma region, a vacuum region, and a number of solid conductor regions. The conductor regions account for the vacuum vessel along with passive conductors and active control coils. Also present are several sensors that measure flux and magnetic fields as a function of time. We will eventually make a number of simplifying assumptions regarding geometry and timescales. However, initially, we present the governing equations in full generality.

We model the dynamics of the plasma using the linear MHD normal mode equation

$$\gamma^2 \rho \xi = \mathbf{F}(\xi) \tag{1}$$

where γ is the linear growth rate, ρ is the plasma mass density, ξ is the plasma displacement from equilibrium conditions, and $\mathbf{F}(\xi)$ is the standard ideal MHD force operator (see, for example, Ref. 15).

The plasma is coupled to the surrounding vacuum-conductor region by the boundary conditions

$$\mathbf{e}_n \times \hat{\mathbf{A}} \,\big|_{S_p} = -(\mathbf{e}_n \cdot \xi)\mathbf{B}_0 \,\big|_{S_p} \tag{2}$$

and

$$\hat{\mathbf{B}}_0 \cdot \nabla \times \hat{\mathbf{A}} \,\big|_{S_p} = \mathbf{B}_0 \cdot \nabla \times (\xi \times \mathbf{B}_0) \,\big|_{S_p} \ . \tag{3}$$

In Eqs. (2) and (3), $\mathbf{e}_n$ is the outward facing unit normal to the plasma surface S_p, $\hat{\mathbf{A}}$ is the perturbed vector potential in the vacuum-conductor region, and $\mathbf{B}_0$ is the equilibrium magnetic field. Equation (2) is the linearized form of the tangential electric field jump condition $[\![\mathbf{e}_n \times \mathbf{E}]\!] = 0$ while Eq. (3) is the linearized form of the pressure balance jump condition $[\![p + B^2/2\mu_0]\!] = 0$.

Perturbed fields in the vacuum-conductor region evolve according to the diffusion equation

$$\gamma\hat{\mathbf{A}} = -\frac{\eta}{\mu_0}\nabla\times\nabla\times\hat{\mathbf{A}} - \nabla\mathcal{V} \tag{4}$$

where η is the resistivity and $\mathcal{V}$ is the perturbed scalar electric potential. The perturbed electric field results from voltages applied to control coils based on magnetics measurements.

B. Derivation of the Variational Principle

In our calculation, the parameter of greatest practical interest is the linearized growth rate γ because it is a direct measure of the stability of the system. As a result, we will derive a variational principle for estimating this quantity. Following the procedure of Gerjuoy et al.[16] we define the functional

$$\begin{aligned}
\gamma_v(\mathcal{S}_t, \mathcal{L}_t) &= \gamma_t + \int_{V_p} \mathbf{L}_{1t}(\mathbf{r}) \cdot \left[\mathbf{F}(\xi_t) - \gamma_t^2\rho\xi_t\right] dV + \\
&\int_{V_v} \mathbf{L}_{2t}(\mathbf{r}) \cdot \left[\nabla\times\nabla\times\hat{\mathbf{A}}_t + \frac{\gamma_t\mu_0}{\eta}\hat{\mathbf{A}}_t + \frac{\mu_0\mathbf{V}(\mathbf{r})}{\eta}\int_{V_v}\mathbf{M}(\mathbf{r}')\cdot\hat{\mathbf{A}}_t(\mathbf{r}')\,dV'\right] dV + \\
&\int_{S_p} L_{3t}(\mathbf{r})\left[\hat{\mathbf{B}}_0\cdot\nabla\times\hat{\mathbf{A}}_t - f\right] dS + \\
&\int_{S_p} L_{4t}(\mathbf{r})\left[\mathbf{B}_0\cdot\nabla\times(\xi_t\times\mathbf{B}_0) - f\right] dS
\end{aligned} \tag{5}$$

where

$$\mathcal{S}_t \equiv (\xi_t, \hat{\mathbf{A}}_t, \gamma_t)$$

represents a set of trial estimates of the exact solutions

$$\mathcal{S} \equiv (\xi, \hat{\mathbf{A}}, \gamma)$$

of the governing equations and

$$\mathcal{L}_t \equiv (\mathbf{L}_{1t}, \mathbf{L}_{2t}, L_{3t}, L_{4t})$$

represents a set of trial estimates for the functions

$$\mathcal{L} \equiv (\mathbf{L}_1, \mathbf{L}_2, L_3, L_4) .$$

At this point, the $\mathcal{L}_t$ are completely undetermined and the $\mathcal{S}_t$ are constrained only by the condition that they satisfy Eq. (2). In addition, for simplicity, we have assumed that $\nabla\mathcal{V}$ is written in the form

$$\nabla\mathcal{V} = \mathbf{V}(\mathbf{r}) \int_{V_v} \mathbf{M}(\mathbf{r}') \cdot \hat{\mathbf{A}}(\mathbf{r}')\, dV' \tag{6}$$

where $\mathbf{V}(\mathbf{r})$ gives the location and magnitude of the applied electric field and $\mathbf{M}(\mathbf{r}')$ indicates where the vector potential is sampled. If, for example, $\mathbf{V}(\mathbf{r}) = V_j\delta(\mathbf{r} - \mathbf{r}_j)\mathbf{e}_\varphi$ and $\mathbf{M}(\mathbf{r}') = \delta(\mathbf{r}' - \mathbf{r}_k)\mathbf{e}_\varphi$, Eq. (6) describes a proportional feedback voltage applied to an axisymmetric filamentary control coil located at $\mathbf{r} = \mathbf{r}_j$ based on a poloidal flux measurement at $\mathbf{r} = \mathbf{r}_k$.

Equation (5) represents a variational principle for the linear growth rate if

1. $\gamma_v(\mathcal{S}_t, \mathcal{L}_t) = \gamma$ whenever $\mathcal{S}_t = \mathcal{S}$, whether or not $\mathcal{L}_t = \mathcal{L}$, and
2. the total first order error $\delta\gamma_v = \gamma_v(\mathcal{S}_t, \mathcal{L}_t) - \gamma$, composed of terms proportional to $\delta\mathcal{S} = \mathcal{S}_t - \mathcal{S}$ and $\delta\mathcal{L} = \mathcal{L}_t - \mathcal{L}$, vanishes.

If these two conditions are satisfied, first order accurate trial estimates $\mathcal{S}_t$ and $\mathcal{L}_t$ yield a second order accurate estimate of γ.

We note that Eq. (5) is very similar in structure to constrained optimization problems from elementary calculus. The governing equations [Eqs. (1) and (4)] and the pressure balance jump condition [Eq. (3)] appear as constraints multiplied by analogs of Lagrange multipliers (the $\mathcal{L}_t$). As a result of this structure, condition (1) above is satisfied by construction.

Condition (2) is verified by first varying γ_v with respect to $\mathcal{S}_t$ and $\mathcal{L}_t$ and then setting the terms proportional to $\delta\mathcal{S}$ and $\delta\mathcal{L}$ individually to zero. We again see that the construction of Eq. (5) automatically guarantees that $\delta\gamma_v/\delta\mathcal{L}$ vanishes. We now must examine the conditions under which $\delta\gamma_v/\delta S$ vanishes. A short calculation shows that this variation can be written in the form

$$\begin{aligned}\delta\gamma_v \;=\; & \delta\gamma_t \left[1 - c\gamma_t \int_{V_p} \xi_t^\dagger \cdot \rho\xi_t \, dV - \frac{c}{2}\int_{V_v} \frac{\hat{\mathbf{A}}_t^\dagger \cdot \hat{\mathbf{A}}_t}{\eta} \, dV\right] + \\ & \frac{c}{2}\int_{V_p} \delta\xi_t \cdot \left[\mathbf{F}(\xi_t^\dagger) - \gamma_t^2 \rho \xi_t^\dagger\right] dV - \\ & \frac{c}{2\mu_0}\int_{V_v} \delta\hat{\mathbf{A}}_t \cdot \left[\nabla\times\nabla\times\hat{\mathbf{A}}_t^\dagger + \frac{\mu_0\gamma_t}{\eta}\hat{\mathbf{A}}_t^\dagger + \mu_0 \mathbf{M}(\mathbf{r})\int_{V_v} \frac{\mathbf{V}(\mathbf{r}')}{\eta} \cdot \hat{\mathbf{A}}_t^\dagger \, dV'\right] dV - \\ & \frac{c}{2\mu_0}\int_{S_p} (\mathbf{e}_n \cdot \delta\xi_t) \left[\hat{\mathbf{B}}_0 \cdot \nabla\times\hat{\mathbf{A}}_t^\dagger - \mathbf{B}_0 \cdot \nabla \times (\xi_t^\dagger \times \mathbf{B}_0)\right] dS\end{aligned} \tag{7}$$

if we set

$$\mathbf{L}_{1t} = \frac{c}{2}\xi_t^\dagger, \quad \mathbf{L}_{2t} = -\frac{c}{2\mu_0}\hat{\mathbf{A}}_t^\dagger, \quad L_{3t} = c\frac{(\mathbf{e}_n \cdot \xi_t^\dagger)}{2\mu_0} = -L_{4t} \tag{8}$$

and if we assume that $\xi_t^\dagger$ and $\hat{\mathbf{A}}_t^\dagger$ are related on the plasma surface according to

$$\mathbf{e}_n \times \hat{\mathbf{A}}_t^\dagger \,|_{S_p} = -(\mathbf{e}_n \cdot \xi_t^\dagger)\mathbf{B}_0 \,|_{S_p} \; . \tag{9}$$

The symbol c represents a normalization that ensures that $\xi^\dagger$ and $\hat{\mathbf{A}}^\dagger$ have the same units as ξ and $\hat{\mathbf{A}}$.

We see from Eq. (7) that $\delta\gamma_v/\delta S = 0$ if

$$\gamma_t^2 \rho \xi_t^\dagger = \mathbf{F}(\xi_t^\dagger) \tag{10}$$

and

$$\gamma_t \hat{\mathbf{A}}_t^\dagger = -\frac{\eta}{\mu_0}\nabla\times\nabla\times\hat{\mathbf{A}}_t^\dagger - \eta\mathbf{M}(\mathbf{r})\int_{V_v} \frac{\mathbf{V}(\mathbf{r}')}{\eta} \cdot \hat{\mathbf{A}}_t^\dagger \, dV' \tag{11}$$

are satisfied along with the natural boundary condition

$$\hat{\mathbf{B}}_0 \cdot \nabla\times\hat{\mathbf{A}}_t^\dagger \,|_{S_p} = \mathbf{B}_0 \cdot \nabla\times(\xi_t^\dagger \times \mathbf{B}_0) \,|_{S_p} \tag{12}$$

and the normalization condition

$$1 \;-\; c\gamma_t \int_{V_p} \rho\xi_t^\dagger \cdot \xi_t \, dV - \frac{c}{2}\int_{V_v} \frac{\hat{\mathbf{A}}_t^\dagger \cdot \hat{\mathbf{A}}_t}{\eta} \, dV = 0 \, . \tag{13}$$

If the $\xi_t^\dagger$ and $\hat{\mathbf{A}}_t^\dagger$ are chosen in accordance with these relations, condition (2) above is satisfied and the proof that Eq. (5) represents a variational principle for γ is completed.

The quantity $\xi^\dagger$ is called the adjoint displacement and $\hat{\mathbf{A}}^\dagger$ is called the adjoint vector potential. These parameters characterize a "mirror-image" system related to the real ξ, $\hat{\mathbf{A}}$ system we are trying to model. Comparing Eqs. (1)-(4) with Eqs. (9), (10)–(12), we see that the adjoint system differs from the real system only with regard to the diffusion equation satisfied in the vacuum-conductor region. Specifically, the feedback electric field in the adjoint system is applied at the *measurement locations of the real system* based on vector potential measurements at the *active coil locations of the real system*. Substituting a more complicated feedback law for Eq. (6) would change the diffusion equations satisfied by the adjoint vector potenial. However, the validity of the variational principle would not be affected.

We close this section by re-writing the variational principle in a more compact and intuitive form. This is accomplished by substituting Eq. (8) into Eq. (5) and using the variational constraint, Eq. (13), to eliminate c and set $\gamma_v = \gamma_t$. We obtain

$$\gamma^2 K(\xi^\dagger, \xi) + U_F(\xi^\dagger, \xi) + U_V(\hat{\mathbf{A}}^\dagger, \hat{\mathbf{A}}) + \gamma U_D(\hat{\mathbf{A}}^\dagger, \hat{\mathbf{A}}) + U_{FB}(\hat{\mathbf{A}}^\dagger, \hat{\mathbf{A}}) = 0 \tag{14}$$

where

$$K(\xi^\dagger, \xi) = \frac{1}{2}\int_{V_p} \rho \xi^\dagger \cdot \xi \, dV \tag{15}$$

is the plasma inertia contribution,

$$U_F(\xi^\dagger, \xi) = -\frac{1}{2}\int_{V_p} \xi^\dagger \cdot \mathbf{F}(\xi)\, dV - \frac{1}{2\mu_0}\int_{S_p} (\mathbf{e}_n \cdot \xi^\dagger)\,[\mathbf{B} \cdot \nabla \times (\xi \times \mathbf{B})]\, dS \tag{16}$$

is the perturbed energy in the plasma region,

$$U_V(\hat{\mathbf{A}}^\dagger, \hat{\mathbf{A}}) = \frac{1}{2\mu_0}\int_{V_v} \nabla \times \hat{\mathbf{A}}^\dagger \cdot \nabla \times \hat{\mathbf{A}}\, dV \tag{17}$$

is the perturbed energy in the vacuum region,

$$U_D(\hat{\mathbf{A}}^\dagger, \hat{\mathbf{A}}) = \frac{1}{2}\int_{V_v} \frac{\hat{\mathbf{A}}^\dagger \cdot \hat{\mathbf{A}}}{\eta}\, dV \tag{18}$$

is the perturbed energy in the conductor regions, and

$$U_{FB}(\hat{\mathbf{A}}^\dagger, \hat{\mathbf{A}}) = \frac{1}{2}\int_{V_v} \frac{\hat{\mathbf{A}}^\dagger \cdot \nabla \mathcal{V}}{\eta}\, dV \tag{19}$$

is the perturbed energy supplied by the feedback coils. Note that we have also dropped the "t" subscripts for clarity.

C. Simplifications for Studying Tokamak Axisymmetric Stability

The existence of a variational principle for the growth rate allows us to construct an efficient numerical solution procedure in a manner quite similar to conventional ideal MHD calculations. Specifically, we represent the plasma displacement with trial functions and solve for the vacuum-conductor region response exactly. Under these assumptions, setting the variations in Eq. (14) with respect to the adjoint quantities to zero yields

$$\gamma^2 K(\delta\xi^\dagger, \xi) + U_F(\delta\xi^\dagger, \xi) + U_B(\delta\xi^\dagger, \hat{\mathbf{A}}) = 0 \tag{20}$$

with

$$U_B(\delta\xi^\dagger, \hat{\mathbf{A}}) = -\frac{1}{2\mu_0}\int_{S_p}(\mathbf{e}_n \cdot \delta\xi^\dagger)\mathbf{B}_0 \cdot \mathbf{e}_n \times (\mathbf{e}_n \times \nabla \times \hat{\mathbf{A}})\, dS\,, \tag{21}$$

$\hat{\mathbf{A}}$ chosen to satisfy Eqs. (2) and (4), and $\hat{\mathbf{A}}^\dagger$ chosen to satisfy Eq. (9).

These equations are valid for arbitrary three-dimensional modes in an arbitrarily shaped plasma in the presence of an arbitrary set of conductors. They are an extension of earlier work, which considered thin, continuous resistive walls and no feedback.[17]

1. Simplification of the fluid and kinetic energies

Much simpler versions of the variational equations, which are suitable for the study of tokamak vertical stability, result if we assume that the plasma equilibrium and mode are toroidally symmetric; that plasma inertial effects are small; and that all conductors can be represented using a set of toroidally symmetric parallelogram cross section rings.

Since the plasma equilibrium is axisymmetric, we can employ a flux coordinate system defined by

$$\mathcal{J}^{-1} = \nabla\theta \times \nabla\phi \cdot \nabla\varphi\,. \tag{22}$$

Since the mode is axisymmetric, we can write the plasma displacement as

$$\xi = \mathcal{J}\,(X\nabla\varphi \times \nabla\theta + Y\nabla\psi \times \nabla\varphi) + ZR^2\nabla\varphi \tag{23}$$

where X, Y, and Z and are functions only of ψ and θ. We write the adjoint displacement in an analogous manner.

When we substitute Eq. (23) into Eq. (2), we find that

$$\mathbf{e}_n \times \hat{\mathbf{A}} \,|_{S_p} = -X \frac{\mathbf{B}_0}{|\nabla\psi|} \,|_{S_p} \; . \tag{24}$$

Therefore, $\hat{\mathbf{A}}$ and, as a consequence, U_B, does not depend on Y and Z. Only the kinetic and fluid energies depend on these quantities. Accordingly, the terms proportional to $\delta Z^\dagger$ and $\delta Y^\dagger$ in Eq. (20) give the Euler-Lagrange equations

$$\frac{\partial}{\partial\theta}\left\{\frac{R^2}{\mathcal{J}}\left[F\frac{\partial}{\partial\psi}\left(\frac{\mathcal{J}X}{R^2}\right)+\frac{\partial}{\partial\theta}\left(\frac{\mathcal{J}FY}{R^2}-Z\right)\right]\right\} = -\mu_0\gamma^2\rho\mathcal{J}R^2 Z\,, \tag{25}$$

$$\Gamma p\frac{\partial}{\partial\theta}\left[\frac{1}{\mathcal{J}}\frac{\partial}{\partial\psi}(\mathcal{J}X)+\frac{1}{\mathcal{J}}\frac{\partial}{\partial\theta}(\mathcal{J}Y)\right] = \gamma^2\rho\left\{Q^2Y + F\mathcal{J}Z\right\} \tag{26}$$

where $p(\psi)$ is the pressure and $F(\psi) = RB_{0\varphi}$ and

$$Q^2 = \left(\frac{\partial R}{\partial\theta}\right)^2 + \left(\frac{\partial Z}{\partial\theta}\right)^2 \tag{27}$$

is the poloidal arc length.

We are interested in modeling instabilities characterized by

$$\gamma \ll \gamma_{MHD} \tag{28}$$

where γ_{MHD}, the ideal MHD growth rate in the absence of a conducting wall, is on the order of the Alfvén frequency. This is the regime where feedback stabilization is feasible. Equation (28) implies that

$$\epsilon \equiv \frac{\mu_0\rho\gamma^2}{B^2} \ll 1\,. \tag{29}$$

We will exploit Eq. (28) by expanding Y and Z in powers of ϵ and solving order by order. To lowest order in ϵ, we can neglect the right hand sides of Eqs. (25) and (26). Then, we can algebraically eliminate Y and Z in favor of X. X and $X^\dagger$, in turn, are represented as a linear combination of trial functions

$$X = \sum_{i=1}^{N} a_i x_i\,, \quad X^\dagger = \sum_{i=1}^{N} a_i^\dagger x_i \tag{30}$$

where the a_i and $a_i^\dagger$ are variational parameters and we use the same basis functions x_i for both the real and adjoint systems. We find finally that

$$\gamma^2 K(\delta\xi^\dagger, \xi) + U_F(\delta\xi^\dagger, \xi) = \mathbf{W}_F \cdot \mathbf{a} \tag{31}$$

where $\mathbf{a}$ is a vector of length N consisting of the variational parameters a_i, the elements of $\mathbf{W}_F$ are given by

$$\begin{aligned} W_{Fij} &= \frac{\pi}{\mu_0}\int_{V_p}\left[\frac{\nabla x_i}{R}\cdot\frac{\nabla x_j}{R} + \frac{F^2}{R^2}\frac{\langle \mathcal{J}x_i/R^2\rangle'\langle \mathcal{J}x_j/R^2\rangle'}{\langle \mathcal{J}/R^2\rangle^2} + \right. \\ &\left. \frac{FF'}{\mathcal{J}}\left(\frac{\mathcal{J}x_i x_j}{R^2}\right)' + \frac{\mu_0 p'}{\mathcal{J}}(\mathcal{J}x_i x_j)' + \mu_0\Gamma p\frac{\langle \mathcal{J}x_i\rangle'\langle \mathcal{J}x_j\rangle'}{\langle \mathcal{J}\rangle^2}\right]\mathcal{J}\,d\psi d\theta\,, \end{aligned} \tag{32}$$

and

$$\langle A\rangle = \frac{1}{2\pi}\int_0^{2\pi} A\,d\theta\,. \tag{33}$$

Equation (32) is analogous to the result obtained by Chu and Miller,[18] showing that the lowest order (resistive) growth rate is dependent only on the component of the displacement perpendicular to the flux surfaces. Nevertheless, for diagnostic purposes, we often need the other components.

We can compute the other components by integrating Eqs. (25) and (26) twice with respect to θ and then requiring periodicity. This gives

$$Z - F\frac{\mathcal{J}Y}{R^2} = FG(\psi,\theta) + \alpha(\psi) \tag{34}$$

$$\mathcal{J}Y = H(\psi,\theta) + \beta(\psi) \tag{35}$$

where

$$G(\psi,\theta) = \int_0^{\theta}\left[\frac{\partial}{\partial\psi}\left(\frac{\mathcal{J}X}{R^2}\right) - \frac{\mathcal{J}}{R^2}\frac{\langle \mathcal{J}X/R^2\rangle'}{\langle \mathcal{J}/R^2\rangle}\right]d\theta' \tag{36}$$

$$H(\psi,\theta) = \int_0^{\theta}\left[\mathcal{J}\frac{\langle \mathcal{J}X\rangle'}{\langle \mathcal{J}\rangle} - \frac{\partial}{\partial\psi}(\mathcal{J}X)\right]d\theta'\,. \tag{37}$$

We determine $\alpha(\psi)$ and $\beta(\psi)$ by requiring periodicity to the first-order (in ϵ) in Y and Z. This leads to the following constraints on the zeroth order quantities:

$$\langle \mathcal{J} R^2 Z \rangle = 0\,, \tag{38}$$

$$\left\langle Q^2 Y + F \mathcal{J} Z \right\rangle = 0\,. \tag{39}$$

Substituting Eqs. (35) and (34) into Eqs. (38) and (39) gives

$$\alpha(\psi) = \frac{F}{\langle \mathcal{J} R^2 \rangle} \langle \mathcal{J}(H + \beta + R^2 G) \rangle \tag{40}$$

and

$$\beta(\psi) = -\frac{\left\langle \mathcal{J} \left\{ \left[\frac{Q^2}{\mathcal{J}^2 F^2} + \left(\frac{1}{R^2} - \frac{\langle \mathcal{J} \rangle}{\langle \mathcal{J} R^2 \rangle} \right) \right] H + \left(1 - \frac{\langle \mathcal{J} \rangle R^2}{\langle \mathcal{J} R^2 \rangle} \right) G \right\} \right\rangle}{\left\langle \mathcal{J} \left(\frac{Q^2}{\mathcal{J}^2 F^2} + \frac{1}{R^2} - \frac{\langle \mathcal{J} \rangle}{\langle \mathcal{J} R^2 \rangle} \right) \right\rangle} \tag{41}$$

thereby fully determining Y and Z. With this full set of components we can then construct the plasma displacement using Eq. (23).

2. Simplification of the vacuum-conductor region energy

Evaluating Eq. (21) in the presence of an arbitrary set of conductors and coils is an extremely complicated procedure. To simplify matters, we assume that all conductors can be represented by a set of ring coils with parallelogram cross-section. This specification still allows great flexibility in modeling complex conductor configurations since, by judicious choice of resistances and self-inductances, arbitrary passive stabilizers and active control coils can be constructed from the smaller rings. In general, the passive conductors are not precisely toroidally symmetric. Consequently, our representation is a toroidal average. To account for asymmetries we can adjust the position of structure or add an external resistance and/or inductance. To make these corrections, we use analytic models and information from 3D electromagnetic codes.

The assumption of purely toroidal current paths implies that there is no perturbed toroidal field in the vacuum. To see this, we note that the perturbed toroidal field can be written

$$\hat{\mathbf{B}}_\varphi = \mu_0 I_{pol} \nabla \varphi \tag{42}$$

where I_{pol}, the poloidal current in the passive structure, is given by

$$\mu_0 I_{pol} = -\frac{2\pi^2 F(\mathcal{J}X/R^2)\,|_{S_p}}{\int_{V_I} dV/R^2}. \tag{43}$$

If there is no closed poloidal current path around the confined plasma, the region of integration in the denominator is the entire vacuum ($V_I = V_v$). In this case, the integral diverges and I_{pol} vanishes leading to no perturbed toroidal field in the vacuum-conductor region.

Given no perturbed toroidal field and the adjoint version of Eq. (23), we can write Eq. (21) as

$$U_B(\delta X^\dagger, \hat{\mathbf{A}}) = \frac{1}{2\mu_0}\int_{S_p} \frac{\delta X^\dagger}{R}\hat{B}_t\, dS \tag{44}$$

where $\hat{B}_t$ is the tangential component of the perturbed field in the vacuum-conductor region which results from the deformation of the plasma and the currents induced in the ring conductors. For purposes of computing $\hat{B}_t$, it is convenient to write the field as

$$\hat{\mathbf{B}} = \nabla\phi + \sum_{k=0}^{K} \mu_0 I_k \nabla\Psi_k \times \nabla\varphi \tag{45}$$

where ϕ is the scalar magnetic potential,

$$\Psi_k = \frac{(RR_k)^{1/2}}{2\pi}\left[\frac{(2-k_k^2)K(k_k) - 2E(k_k)}{k_k}\right], \tag{46}$$

$K(k)$ and $E(k)$ are the complete elliptic integrals, and

$$k_k^2 = \frac{4RR_k}{(R+R_k)^2 + (Z-Z_k)^2}. \tag{47}$$

The second term in Eq. (45) accounts for the perturbed conductor currents ($k \neq 0$) and the perturbed plasma current ($k = 0$). In the latter case, (R_0, Z_0) is any point inside the plasma, typically the location of the magnetic axis.

Since the fields due to all currents are explicitly accounted for, ϕ simply satisifies Laplace's equation, which can efficiently be solved using Green's theorem.[20–22] The axisymmetric form of Green's theorem is written

$$\frac{1}{2}\phi(\theta) + \int_0^{2\pi}\left[\phi(\theta')\frac{\partial G}{\partial n'}(\theta,\theta') - G(\theta,\theta')\frac{\partial \phi}{\partial n'}(\theta')\right] R'\, d\theta' = 0 \tag{48}$$

where both observation (un-primed) and integration (primed) quantities are parameterized in terms of our poloidal angle variable θ. The Green's function in this case is

$$G = -\frac{kK(k)}{2\pi(RR')^{1/2}} \tag{49}$$

where

$$k^2 = \frac{4RR'}{(R+R')^2 + (Z-Z')^2} \tag{50}$$

and the normal derivative of ϕ is defined

$$R\frac{\partial\phi}{\partial n} = Q\mathbf{e}_n \cdot \nabla\phi\,. \tag{51}$$

Equation (48) has the solution

$$\phi(\theta) = \int_0^{2\pi} T(\theta,\, \theta')R'\frac{\partial\phi}{\partial n'}\,d\theta'\,. \tag{52}$$

The function T can be calculated by expanding ϕ and $R\,\partial\phi/\partial n$ in Fourier series involving θ. Then,

$$T(\theta,\, \theta') = \frac{1}{2\pi}\sum_{m=-M}^{M}\,\sum_{m'=-M}^{M} T_{mm'}e^{im\theta - im'\theta'} \tag{53}$$

and

$$\mathbf{T} = [\mathbf{I} + \mathbf{A}]^{-1} \cdot \mathbf{C}\,. \tag{54}$$

In Eq. (54), $\mathbf{I}$ is the identity matrix. The elements of $\mathbf{A}$ and $\mathbf{C}$ are given by

$$A_{mm'} = \frac{1}{\pi}\int_0^{2\pi}\int_0^{2\pi}\left(R\frac{\partial G}{\partial n'}\right)e^{im'\theta' - im\theta}\,d\theta\,d\theta' \tag{55}$$

and

$$C_{mm'} = -\frac{1}{\pi}\int_0^{2\pi}\int_0^{2\pi} Ge^{im'\theta' - im\theta}\,d\theta\,d\theta'\,. \tag{56}$$

These matrix elements can be efficiently computed using fast Fourier transforms. Note that special care must be exercised to correctly handle the integrable logarithmic singularies present in Eqs. (55) and (56).[20]

The perturbed field $\hat{\mathbf{B}}$ must satisfy Eq. (24) on the plasma surface and must also vanish at infinity. Using Eq. (45), we can therefore derive a relation for the normal derivative of ϕ on the plasma surface,

$$R\frac{\partial \phi}{\partial n} = \frac{\partial}{\partial \theta}\left(X + \sum_{k=0}^{K} \mu_0 I_k \Psi_k \right) . \tag{57}$$

Substituting Eqs. (30), (52), and (57) into Eq. (44) yields

$$U_B = \mathbf{W}_V \cdot \mathbf{a} + \mathbf{W}_W \cdot \mathbf{i} , \tag{58}$$

with

$$\mathbf{W}_V = -\frac{\pi}{\mu_0}\left(\int_0^{2\pi} \int_0^{2\pi} \frac{\partial \mathbf{x}}{\partial \theta} T(\theta,\, \theta') \frac{\partial \mathbf{x}}{\partial \theta'}\, d\theta d\theta' - \boldsymbol{\Omega}_a\, D^{-1}\, \boldsymbol{\Omega}_a \right) \tag{59}$$

and

$$\mathbf{W}_W = \frac{\pi}{\mu_0}\left(\int_0^{2\pi} \left[\frac{\mathbf{x}}{R}\frac{\partial \boldsymbol{\Psi}}{\partial n} - \int_0^{2\pi} \frac{\partial \mathbf{x}}{\partial \theta} T(\theta,\, \theta') \frac{\partial \boldsymbol{\Psi}}{\partial \theta'} \right] d\theta - \boldsymbol{\Omega}_a\, D^{-1}\, \boldsymbol{\Omega}_i \right) . \tag{60}$$

Here, $\mathbf{i}$ and $\boldsymbol{\Psi}$ are vectors of length K consisting of the $\mu_0 I_k$ and the Ψ_k for the external conductors only. We have eliminated the perturbed plasma current using the relation

$$\mu_0 I_0 D = \boldsymbol{\Omega}_a \cdot \mathbf{a} + \boldsymbol{\Omega}_i \cdot \mathbf{i} . \tag{61}$$

To obtain $\boldsymbol{\Omega}_a$, $\boldsymbol{\Omega}_i$, and D, we require an equation for the perturbed flux, which we turn to next. But first, we note that Eq. (59), represents the perturbed vacuum energy due to the plasma surface's deformation and must be symmetric. This, in turn, implies that $T(\theta,\, \theta')$ must equal $T(\theta',\, \theta)$. Hence, $\mathbf{T}$ must be Hermitian. This symmetry is somewhat surprising in view of Eqs. (55) and (56) which display no readily apparent symmetry properties. As a result, the symmetry property of $\mathbf{T}$ represents a good check of the numerical procedures used to implement our models. Equation (60) contains the stabilizing effect of the "wall" made up of the external conductors.

3. Simplification of the circuit equations

Given our assumptions, Eq. (4) turns into K equations, one for each external conductor; namely,

$$2\pi\gamma\hat{\psi}_k + r_k I_k = V_k \tag{62}$$

where $\hat{\psi}_k$, r_k, and V_k are respectively the flux, resistance, and applied voltage at the kth conductor located at $\mathbf{r}_k = (R_k, Z_k)$.

The perturbed poloidal flux in the vacuum-conductor region can be written

$$\hat{\psi} = \tilde{\psi} + \sum_{k=0}^{K} \mu_0 I_k \Psi_k \tag{63}$$

where $\tilde{\psi}$ satisfies $\Delta^*\tilde{\psi} = 0$. Accordingly, $\tilde{\psi}$ can be determined at an arbitrary location in the vacuum by using the version of Green's theorem valid for the vector potential:

$$\tilde{\psi}_k = \int_0^{2\pi} \left[\frac{\tilde{\psi}(\theta')}{R'} \frac{\partial \Psi_k}{\partial n'} - \frac{\Psi_k}{R'} \frac{\partial \tilde{\psi}}{\partial n'} \right] d\theta' . \tag{64}$$

The integral is evaluated on the plasma surface where $\hat{\psi} = -X$. Also, from Eq. (45) and Eq. (63) we have

$$\frac{\partial \tilde{\psi}}{\partial n} = R \frac{\partial \phi}{\partial \theta} , \tag{65}$$

which, when substituted into Eq. (64) along with Eqs. (63) and (61), generates

$$2\pi\hat{\psi}_k = \sum_{i=1}^{N} P_{ki} a_i + \sum_{l=0}^{K} L_{kl} i_l \tag{66}$$

where

$$\mathbf{P} = -2\pi \left(\int_0^{2\pi} \left[\frac{\partial \Psi}{\partial n} \frac{\mathbf{x}}{R} - \int_0^{2\pi} \frac{\partial \Psi}{\partial \theta} T(\theta, \theta') \frac{\partial \mathbf{x}}{\partial \theta'} \, d\theta' \right] d\theta + \mathbf{\Omega}_i D^{-1} \mathbf{\Omega}_a \right) \tag{67}$$

and

$$\mathbf{L} = \mathbf{M} - 2\pi \left(\int_0^{2\pi} \left[\frac{\Psi}{R} \frac{\partial \Psi}{\partial n} - \int_0^{2\pi} \frac{\partial \Psi}{\partial \theta} T(\theta, \theta') \frac{\partial \Psi}{\partial \theta'} \, d\theta' \right] d\theta - \mathbf{\Omega}_i D^{-1} \mathbf{\Omega}_i \right) . \tag{68}$$

$\mathbf{P}$ represents the perturbed inductance due to the plasma surface deformation, while $\mathbf{L}$ represents the inductive coupling between the conductors in the presence of the plasma. The first term in Eq. (68) is simply the vacuum mutual inductance matrix whose off-diagonal elements are $M_{kl} = 2\pi\Psi_k|_{\mathbf{r}=\mathbf{r}_l}$. The diagonal (self-inductnce) elements of $\mathbf{M}$ are given using an analytic approximation for parallelogram coils.

The derivation of Eqs. (67) and (68) required use of the symmetry property of $T(\theta, \theta')$ and repeated use of Eq. (63). We can immediately see the symmetry of $\mathbf{L}$; furthermore, we have the symmetry relation $\mathbf{P} = -2\mu_0 \mathbf{W}_W^T$.

4. Accounting for the perturbed plasma current

We compute the perturbed plasma current by evaluating, $\int dV \nabla\Psi_0 \times \nabla\varphi \cdot \hat{\mathbf{B}}$ over the vacuum region using first Eq. (63) and then Eq. (45). This gives

$$\int_0^{2\pi} \frac{X}{R}\frac{\partial\Psi_0}{\partial n}\, d\theta = \int_0^{2\pi} \left[\phi(\theta)\frac{\partial\Psi_0}{\partial\theta} - \sum_{k=0}^{K} \mu_0 I_k \frac{\Psi_k}{R}\frac{\partial\Psi_0}{\partial n}\right] d\theta. \tag{69}$$

Then, using Eq. (52), we can identify

$$\Omega_i = -\int_0^{2\pi} \left[\frac{\Psi}{R}\frac{\partial\Psi_0}{\partial n} - \int_0^{2\pi} \frac{\partial\Psi}{\partial\theta'} T(\theta, \theta')\frac{\partial\Psi_0}{\partial\theta'}\, d\theta'\right] d\theta \tag{70}$$

and

$$\Omega_a = -\int_0^{2\pi} \left[\frac{\mathbf{x}}{R}\frac{\partial\Psi_0}{\partial n} - \int_0^{2\pi} \frac{\partial\mathbf{x}}{\partial\theta'} T(\theta, \theta')\frac{\partial\Psi_0}{\partial\theta'}\, d\theta'\right] d\theta\,, \tag{71}$$

and

$$D = \int_0^{2\pi} d\theta \left[\frac{\Psi_0}{R}\frac{\partial\Psi_0}{\partial n} - \int_0^{2\pi} d\theta' \frac{\partial\Psi_0}{\partial\theta} T(\theta, \theta')\frac{\partial\Psi_0}{\partial\theta'}\right]. \tag{72}$$

Notice that only one relation was needed to compute I_0, whereas continuity of flux across the plasma boundary (which was used to compute I_0) must be satisfied at all points on the plasma boundary. Consequently, this property serves as a check on the accuracy and validity of the computation. Of course, for up/down symmetric plasmas, the perturbed plasma current is zero by symmetry for the unstable mode and this check is lost.

D. Summary and Discussion

From the expressions for the fluid energy Eq. (31) and the vacuum energy Eq. (58), we can form the energy balance equation

$$(\mathbf{W}_F + \mathbf{W}_V) \cdot \mathbf{a} + \mathbf{W}_W \cdot \mathbf{i} = 0\,. \tag{73}$$

From the circuit equations we can write

$$(\gamma \mathbf{L} + \mathbf{R}) \cdot \mathbf{i} - 2\mu_0 \gamma \mathbf{W}_W^T \cdot \mathbf{a} = \mathbf{V} \tag{74}$$

where $\mathbf{R}$ is the resistance matrix. These two matrix equations describe the vertical stability properties of our system.

We can construct the ideal energy principal from Eqs. (73) and (74) by neglecting the resistance and the applied voltage. We then eliminate $\mathbf{i}$ to obtain

$$\left(\mathbf{W}_F + \mathbf{W}_V + 2\mu_0 \mathbf{W}_W \mathbf{L}^{-1} \mathbf{W}_W^T\right) \cdot \mathbf{a} = (\mathbf{W}_\infty + \mathbf{W}_{wall}) \cdot \mathbf{a} = 0\,. \tag{75}$$

We immediately see the stabilizing contribution of the wall, $\mathbf{W}_{wall}$, and we note that, as expected, the number of eigenmodes is equal to the number of trial functions.

In the general case involving resistance and feedback we eliminate $\mathbf{a}$. This yields

$$\gamma \left[\mathbf{L} + 2\mu_0 \mathbf{W}_W^T \mathbf{W}_\infty^{-1} \mathbf{W}_W\right] \cdot \mathbf{i} + \mathbf{R} \cdot \mathbf{i} = [\gamma \mathcal{L} + \mathbf{R}] \cdot \mathbf{i} = \mathbf{V}\,. \tag{76}$$

We write the applied voltage $\mathbf{V}$ in the form of a proportional-derivative-integral (PDI) control law

$$\mathbf{V} = \frac{\kappa}{\kappa + \gamma} (\mathbf{G}_P + \gamma \mathbf{G}_D) \cdot \zeta + \frac{1}{\gamma} \mathbf{G}_I \cdot \zeta\,, \tag{77}$$

where ζ is the measurement, the $\mathbf{G}$'s are the respective gain matrices, and κ is the frequency width of a low band filter.

To close the problem, we need to express $\mathbf{V}$ as a linear function of $\mathbf{i}$. For flux loop measurements this is accomplished by writing

$$\zeta = \mathcal{L}' \cdot \mathbf{i} \tag{78}$$

where $\mathcal{L}'$ is computed in a manner identical to $\mathcal{L}$ except that fluxes are evaluated at the loop locations. In the case of measurements of the magnetic axis

$$\zeta = -\left\langle \frac{\partial \mathbf{x}}{\partial \bar{\rho}} \right\rangle |_{\bar{\rho}=0} \cdot \mathbf{W}_{\infty}^{-1} \cdot \mathbf{W}_W \tag{79}$$

where $\bar{\rho}$ is a radius-like variable in the polar coordinate system

$$R = R_{axis} + \bar{\rho}(\psi, \theta) \cos(\theta) \, , Z = Z_{axis+} \kappa_0 \bar{\rho}(\psi, \theta) \sin(\theta) \, . \tag{80}$$

Here κ_0 is the ellipticity of the magnetic axis.

For the purely passive system, $\mathbf{V} = 0$, Eq. (76) is a generalized eigenvalue system. The matrices in this linear system are all symmetric and, therefore, the eignevalues, γ, are all real. The number of eigenmodes is equal to K, the number of conductors. This corresponds to the number of modes resolved from a continuous resistive wall. Recall that we have assumed throughout this paper that conductors are close enough to give ideal MHD stability in the limit in which they are perfect conductors. Thus, all that remains is the slow instability due to flux leakage through the resistive wall. There is at most one unstable mode; all others are damped. In the limit in which the ideal MHD energy is zero, the growth rate approaches infinity. This is due to the breakdown of the assumption that inertia can be neglected. This regime must be avoided in the analysis (and in practical designs).

With the addition of an applied voltage, the matrices are no longer symmetric and complex eigenfrequencies can now occur in conjugate pairs. The number of eigenmodes can also increase. For the feedback law defined in Eq. (77) additional modes come about because of the low pass filter and the integral feedback which must be handled by writing $\mathbf{V} = \mathbf{V}_1 + \mathbf{V}_2$ where

$$\kappa (\mathbf{G}_P + \gamma \mathbf{G}_D) \cdot \zeta = (\kappa + \gamma) \mathbf{V}_1 \, , \tag{81}$$

$$\mathbf{G}_I \cdot \zeta = \gamma \mathbf{V}_2 \, . \tag{82}$$

Equations (81) and (82) are added to the set Eq. (76) to give an augmented generalized eigenvalue problem $\gamma \mathbf{A} \cdot \mathbf{y} = \mathbf{B} \cdot \mathbf{y}$ where $\mathbf{y} = \{\mathbf{i}, \mathbf{V}_1, \mathbf{V}_2\}$.

A complete gap controller, though more complicated, follows the same logic. Here, we have

$$\mathbf{V} = \mathbf{G}_x \cdot \mathbf{X} + (\mathbf{G}_P + \gamma \mathbf{G}_D) \cdot \mathbf{h} \, , \tag{83}$$

where h is a vector that contain the gap errors, the error in the desired plasma current, and the errors in the coil currents. The state space vectors, $\mathbf{X}$ satisfy

$$\gamma \mathbf{X} = \mathbf{M} \cdot \mathbf{X} + (\mathbf{H}_P + \gamma \mathbf{H}_D) \cdot \mathbf{h}. \tag{84}$$

One further point with regard to this equation set. In general there would be no explicit derivative gains; Eq. (84) can generate derivative like gains from the proportional gain sources.

III. Numerical Issues

We consider two classes of trial functions. One is local, based on B-splines.[19] In this representation, the x_i are chosen from the set

$$\begin{aligned} &\bar{\psi}^{1/2} B_m(\bar{\psi}) \left\{ \begin{array}{c} \cos l\theta \\ \sin l\theta \end{array} \right\}, \quad l = odd;\ m = 1, 2, \ldots \\ &\bar{\psi} B_m(\bar{\psi}) \left\{ \begin{array}{c} \cos l\theta \\ \sin l\theta \end{array} \right\}, \quad l = even;\ m = 1, 2, \ldots \end{aligned} \tag{85}$$

where $B_m(\bar{\psi})$ is the mth B-spline basis function and

$$\bar{\psi} = \frac{\psi - \psi_{axis}}{\psi_{edge} - \psi_{axis}}. \tag{86}$$

The second trial function set is global in nature. Here, the x_i are chosen from the set

$$\begin{aligned} &l \bar{\psi}^{l/2} \left\{ \begin{array}{c} \cos l\theta \\ \sin l\theta \end{array} \right\}, \quad l = 1, 2, \ldots;\ m = 0; \\ &l J_l(\Lambda_{l,m} \bar{\psi}) \left\{ \begin{array}{c} \cos l\theta \\ \sin l\theta \end{array} \right\}, \quad l = 1, 2, \ldots;\ m = 1, 2, \ldots; \end{aligned} \tag{87}$$

where $\Lambda_{l,m}$ is the mth zero of the Bessel function J_l. Following Chu and Miller,[18] we can also substitute the rigid vertical and horozontal shifts

$$x_Z = \frac{\partial \psi}{\partial Z}, x_R = \frac{\partial \psi}{\partial R} \tag{88}$$

for the $l = \pm 1$, $m = 0$ global trial function. Both sets of trial functions use the θ coordinate defined in Eq. (80).

We have implemented the procedure described in the previous sections as a module of the free-boundary equilibrium code, TEQ. This direct coupling is convenient because of the large amount of equilibrium information needed to perform vertical stability calculations. In addition, TEQ possesses an interactive, programmable shell that greatly facilitates the examination of parameter space.

When we examine vertical stability with the TEQ code, we calculate the fluid energy integral using a radial grid consisting of approximately 80–120 flux surfaces and an angular grid consisting of approximately 120 points. The radial grid is non-uniform: more surfaces are placed in the vicinity of the magnetic axis and the plasma edge. This non-uniform grid is particularly important at low ℓ_i where the current profile is steep at the edge. In these cases, we find that, with an equally spaced grid, more than 1000 flux surfaces can be required for convergence.

We typically truncate the Fourier series in Eq. (53) at $|M| = 48$. This number of harmonics allows us to model plasmas with surface fluxes characterized by $\theta_c = 0.001$. θ_c is a measure of the proximity of the separatrix surface. It is defined $\theta_c = (\psi_X - \psi_P)/(\psi_P - \psi_0)$ where ψ_X is the flux label of the nearest separatrix surface, ψ_P is the flux label of the plasma surface, and ψ_0 is the flux value at the magnetic axis.

The number of conductors in the vacuum region depends on the complexity of the resistive structure and the proximity of the plasma to the structure. Generally, the separation between adjacent conductors must be less than their distance to the plasma surface. For most ITER and TPX cases, we find that a hundred conductors is quite adequate.

Since our procedure is variational, convergence of the growth rate with respect to the number of trial functions is an important issue. Figure 1 shows how the growth rate varies as a function of the number of B-splines (m-values) and harmonics (l-values) in Eq. (85) for an up/down symmetric TPX plasma with $\theta_c = 0.001$. We see the the answer has essentially converged with 10 nodes and 10 harmonics (a total of 100 trial functions). Convergence for single-null plasmas is slower. In this case, we can require as many as 25 nodes and 25 harmonics (giving a total of 450 trial functions since both sines and cosines must be used). The large number of trial functions needed for convergence is a direct result of the X-point. Limited plasmas can require fewer than 10 trial functions. Convergence with the number of trial functions has also been demonstrated for feedback. Here our figure of merit would be the convergence of coil currents and coil voltages.

For strongly-shaped equilibria, we generally find that the B-spline trial functions are superior to the Bessel function trial functions in that they require fewer equilibrium flux surfaces and show better convergence properties.

Our implementation is fast. It typically requires less than a minute to compute vertical stability properties for a single null plasma on a standard workstation. Also, by virtue of the fact that we are solving linear systems, the code never fails to produce an answer.

IV. Applications

We have used the TEQ vertical stability package to consider a number of issues associated with the TPX and ITER designs. In this section, we will describe three of these applications:

- β_p-ℓ_i stability surveys.
- Single null versus double null stability.
- Feedback system design.

While discussing these applications, we will present results from other codes to provide corraboration to the TEQ predictions.

A. β_p-ℓ_i Stability Surveys

During the ITER conceptual design activity (CDA), we found that it was useful to plot vertical stability as a function of poloidal beta and normalized internal inductance. Since the plasma shape is held fixed during the plasma burn, this information allows us to assess stability at various points in the burn. For instance, β_p is small at the start of the burn and $\beta_p \approx 1$ during the flat-top. During flat-top ℓ_i is near unity; however, during off-normal events such as a beta collapse, both β_p and ℓ_i drop.

Figure 2 shows a β_p-ℓ_i survey for TPX. We see that the passive growth rate decreases as β_p increases. This result is due to the Shafranov shift of the equilibrium flux surfaces. As β_p increases, the shift increases and the current centroid moves closer to the vacuum vessel wall. This increases the image currents induced in the wall. These currents act to retard the plasma motion so the growth rate decreases.

The variation in growth rate with respect to ℓ_i is more interesting. As Fig. 2 shows, there is actually a minimum in the growth rate as ℓ_i increases at fixed β_p. The increase in the growth rate at higher ℓ_i values is well known. It is due to the fact that broadening of the current profile brings current closer to the stabilizing vacuum vessel. The increase in growth rate as ℓ_i decreases at lower ℓ_i values was a somewhat surprising effect first predicted by the TEQ code.

This behavior is affected by the geometry of the conducting structure. For example, the ITER engineering design activity (EDA) device does not display a minimum in ℓ_i because of the close proximity of the conducting structure.

We subsequently confirmed our results by comparing with the GATO ideal MHD code. Since GATO computes growth rates for ideal MHD instabilities and TEQ computes growth rates for resistive wall instabilities, we could compare the two codes directly only at marginal stability. Moreover, GATO is only capable of handling relatively simple wall geometries. Accordingly, we considered the idealized case of a strongly shaped ($\delta \approx 0.8$, $\kappa \approx 1.8$) and diverted ($\theta_c = 0.001$) double null plasma surrounded by an elliptical conducting wall. We found that both codes displayed a maximum in the marginal wall position, indicating a minimum in passive growth rate, at about the value of ℓ_i. Other codes have subsequently confirmed this behavior. More recently this same result was published by Ward, Bondeson, and Hofmann.[14]

B. Single Null Versus Double Null Stability

Examination of Eq. (32) suggests that single null plasmas might be inherently more stable than double null plasmas. Double null plasmas are characterized by anti-symmetric displacements. As a result, the second (toroidal field bending) and the fifth (compression) terms integrate to zero, independent of X. On the other hand, these terms do not automatically vanish in a single null plasma. Moreover, these terms, particularly the toroidal field bending energy, represent large stabilizing effects. Therefore, the variational principle will adjust the displacement to minimize these terms. Specifically, the variational principle predicts that X will be driven toward zero in the vicinity of the X-point of a single null plasma. Constraints on the displacement such as this tend to increase the stability of the plasma.

In Fig. 3, we plot γ as a function of θ_c for the double null TPX baseline plasma and two single null configurations, one more asymmetric than the other. Notice that, at low values of θ_c, the single null plasmas are, indeed, more stable. Moreover, the stability improves as the plasma asymmetry increases. One would expect that the difference in stability between single null and double null configurations would decrease as θ_c increases because the effect of the X-points gets smaller as the plasma surface moves away from them. This is shown in Fig. 3 as well. At larger values of θ_c (> 0.02), the behavior becomes dominated by equilibrium differences. Therefore, the fact that the curves in Fig. 3 cross is not significant.

We see in Fig. 4a, which displays contours of the perturbed flux X for the TPX double null plasma, that X indeed remains finite in the vicinity of the separatrix surface. This is in contrast to the single null result shown in Fig. 4c, which clearly shows X vanishing near the X-point, which is at the bottom of the plasma.

Substituting X and Y into Eq. (23), yields an "arrow" diagram showing the plasma displacement at each point inside the plasma. Arrow diagrams for the double and single null plasmas are shown in Figs. 4b and 4d respectively. We see from Fig. 4b that the displacement of the double null plasma is strongly peaked toward the plasma surface. Moreover, the movement is not completely vertical: the flow is directed toward the the X-point. This is consistent with X remaining finite in the vicinity of the separatrix surface. In the case of the single null, the flow is much more rigid. This is consistent with X vanishing in the vicinity of the separatrix surface.

Equation (23) implies that if X is finite, the displacement and hence the kinetic energy would be large in the vicinity of the X-point. Recall that we formally ordered the kinetic energy term small in our calculation and, in fact, it does not even appear in the computation of X. Therefore, one might think that calculations that do include the full kinetic energy contribution could predict a different set of X contours. This is not the case. Both the Nova-W[23] and the GATO codes predict finite X near the separatrix surface for double null plasmas. To accomplish this and still keep the kinetic energy bounded, a narrow boundary layer must be set up in those codes to force X to zero at the X-point.

Finally, in Fig. 5, we show the perturbed flux outside of a single null plasma. We see first that flux is continuous (as promised in Section III) and second, that there is a discontinuity in $\partial\psi/\partial n$ at the surface, primarily near the X-point. This indicates a surface current. This current cancels top-to-bottom for up/down symmetric plasmas.

C. Feedback System Design

Let us illustrate feedback system design capabilities of the TEQ vertical stability module using the ITER EDA plasma configuration shown in Fig. 6.

In this section, we present time traces of perturbed quantities such as currents and voltages. These traces are dervied starting with Eq. (76). For simplicity, we limit this treatment to just a proportional-derivative (PD) contoller without filtering. In this case the number of modes is just the number of conductors, active and passive. We then vary the gains to find an "optimal" system similar to the critically damped limit of a single mode system. In general, this will correspond to the fastest recovery with minimum power and minimal ringing. Having done this, we then have a set of eigennfunctions and eigenvalues of this system. We wish to trace the the time evolution from an initial unstable displacement. Therefore, the currents in all the conductors associated with unstable mode of the purely passive system, $V = 0$, is the initial condition. We next find the linear combination of modes in the feedback system $V \neq 0$ which corresponds to this state at $t = 0$. Next, we need only multiply each mode by $\exp(\gamma_k t)$ and sum over the modes, k; and we have the complete time history.

We have examined the three methods of feedback control displayed in Eqs. (78)-(84). In the first, we measure the perturbed flux asymmetry from a pair of coils located between the inboard passive structure and the plasma, denoted by the $\times$'s in Fig. 6. We use this measurement to drive a pair of coils (labelled 2 and 7 in Fig. 6) with opposite signs of the voltage. Note that this is slightly artificial in that, normally, all of the shaping coils would be used to provide the control. We use the feedback control law shown in Eq. (81) with proportional and derivative gains in approximately equal amounts. This is roughly optimal since the passive growth rate is of order 1 sec. We note from Fig. 7 that equilibrium conditions (zero displacement) is achieved in about 2 seconds (a design requirement) and that the voltages and currents for this 1 cm initial displacement are well within ITER requirements (300 MW total power and 200 MW/sec $\dot{P}$) when scaled to 10 cm.

In a second example, we use a measurement of the vertical displacement of the magnetic axis to drive the same pair of control coils. This example is shown in Fig. 8. Comparing Fig. 7 and Fig. 8, we see that the time behavior for the two cases are quite similar, with perhaps less ringing in Fig. 8.

As a final example we show the results of an ITER controller,[13] which is designed to control the position and shape of the plasma boundary and the plasma current. Here the measurements are six position, or "gap," errors around the plasma boundary. (See Fig. 6 and note that gap positions 1 and 2 are strike points on the divertor plate.) The coil currents and the plasma current are also measured. These measurements are then fed into the contoller plant (not described here) and the resultant voltages are applied to the complete set of coils. As Fig. 9 shows, we see a substantial amount of ringing. The linear model which produced this controller was an approximation to the ideal MHD model we have developed; perhaps the most important difference is the absence of skin currents in the approximate linear model. These currents are generated as the plasma moves. Had we included resistive effects, these currents would have diffused over a local skin depth. Thus, their influence should still be felt, but probably reduced. Of course, these effects are also present in the non-linear codes described in the introduction. It is imjportant to note that these skin-like currents would not be expected to be as important for global control such as vertical control, plasma current control, or elongation control as compared with the gap control being implemented in ITER. This latter point a direct consequence of the proximity of the gap positions to the plasma boundary.

V. Summary and Conclusions

We have developed a variational procedure for determining general 3D MHD stability in the presence of resistive conductors and feedback. We have applied this formalism to axisymmetric configurations appropriate for the study of tokamak vertical stability. We have also developed a perturbation method for generating the other components of the plasma displacement from the variationally determined normal component.

An extremely useful product of this work is a stability module, tightly integrated with TEQ, a general purpose axisymmetric equilibrium code. This package is fast, versatile, and robust: it requires under a minute to compute vertical stability for up/down asymetric equilibria on a standard workstation, it can directly evaluate the stability properties of any TEQ equilibria and any passive structure/feedback system configuration, and it never fails.

This code has identified interesting vertical stability behavior including the non-monotonic variation in growth rate with respect to internal inductance and the greater stability of single-null configurations. It has been heavily used in the design of ITER (both the CDA and the EDA) and the design of TPX.

This work could be extended in several interesting directions. First, a boundary layer analysis could possibly be used to incorporate edge resistive plasma effects into the model. Second, the general 3D variational principle could be applied to non-axisymmetric modes in order to consider feedback stabilization of kink modes. Finally, the vacuum/conductor region modeling could be extended to allow for poloidal current paths.

Acknowledgments

This work was performed under the auspices of the U.S. Department of Energy by Lawrence Livermore National Laboratory under Contract W–7405–ENG–48. We would like to thank Dave Humphreys of General Atomics for many fruitful collaborations on vertical stability issues and Alan Turnbull of General Atomics for help with the GATO stability code.

References

[1]S.C. Jardin, N. Pomphrey, J. De Lucia, J. Comput. Phys. **66** (1986) 481.

[2]J.A. Crotinger, R.H. Cohen, S.W. Haney, L.L. LoDestro, A.I. Shestakov, G.R. Smith, L.D. Pearlstein, T.D. Rognlien, and A.G. Tarditi, Bull. Am. Phys. Soc. **38** (1993) 2016.

[3]A.G. Tarditi, R.H. Cohen, J.A. Crotinger, G.D. Porter, T.D. Rognlien, A.I. Shestakov, and G.R. Smith, Contrib. Plasma Phys. **36** (1996) 132.

[4]R.R. Khayrutdinov, V.E. Lukash, J. Comput. Phys. **109** (1993) 193.

[5]D.J. Ward, S.C. Jardin, Nucl. Fus. **32** (1992) 973.

[6]D. Berger, L.C. Bernard, R. Gruber, and F. Troyon, *Plasma Physics and Controlled Fusion Research* (International Atomic Energy Agency, Vienna, 1976), Vol. II, 411.

[7]R. Gruber, F. Troyon, D. Berger, L.C. Bernard, S. Rousset, R. Schreiber, W. Kerner, W. Schneider, and K.V. Roberts, Comput. Phys. Commun. **21** (1981) 323.

[8]D.A. Humphreys, I.H. Hutchinson, MIT Plasma Fusion Center Report PFC/JA-89-28, Mass. Inst. of Tech., Cambridge, (1989).

[9]D.A. Humphreys, I.H. Hutchinson, Fus. Tech. **23** (1993) 167.

[10]I.H. Hutchinson, Nucl. Fus. **29** (1989) 2107.

[11]D.A. Humphreys, R.H. Bulmer, S.W. Haney, A.G. Kellman, J.A. Leuer, L.D. Pearlstein, Fus. Tech. **26** (1994) 331.

[12]D.A. Humphreys, R.H. Bulmer, S.W. Haney, A.G. Kellman, J.A. Leuer, L.D. Pearlstein, A. Portone, Proc. 18th Symp. on Fus. Technol., Karlsruhe, Germany, August 1994, **1** (1995) 731.

[13]A. Portone, Y. Gribov, M. Huguet, P.L. Mondino, R. Albanese, D.A. Humphreys, C. Kessel, L.D. Pearlstein, J. Wesley, to be published in Fus. Tech. **31** (1997).

[14]D.J. Ward, A. Bondeson, and F. Hofmann, Nucl. Fus. **33** (1993) 831.

[15]J.P. Freidberg, *Ideal Magnetohydrodynamics* (Plenum, New York, 1987).

[16]E. Gerjuoy, A.R.P. Rau, and L. Spruch, Rev. Mod. Phys. **55**, (1983) 725.

[17]S.W. Haney and J.P. Frediberg, Phys. Fluids B **1** (1989) 1637.

[18]M.S. Chu and R.L. Miller, Phys. Fluids **21**, (1978) 817.

[19]A. Watt, *Three-Dimensional Computer Graphics,* (Addison-Wesley, Wokingham, England, 1989) 123.

[20]J.P. Freidberg and F.A. Haas, Phys. Fluids **17**, (1974) 440.

[21]J.P. Freidberg and W. Grossman , Phys. Fluids **18**, (1975) 1494.

[22]J.P. Freidberg, W. Grossman, and F.A. Haas, Phys. Fluids **19**, (1976) 1599.

[23]D.J. Ward, private communication, 1991.

Figure Captions

1. Variation of passive growth rate γ [Hz] with respect to the number of B-spline basis functions and the number of harmonics for an up/down symmetric TPX plasma characterized by a relative X-point proximity $\theta_c = 0.001$.

2. Variation of passive growth rate γ [Hz] with respect to normalized internal inductance ℓ_i and poloidal beta β_p for an up/down symmetric TPX plasma characterized by a relative X-point proximity $\theta_c = 0.001$.

3. Variation of passive growth rate γ [Hz] for a double null TPX plasma (squares), a single null TPX plasma (circles), and a more asymmetric single null TPX plasma (triangles) as a function of the relative X-point proximity $\theta_c = 0.001$.

4. Perturbed plasma flux contours and displacement arrows for double null and single null TPX plasmas: (a) variation in perturbed flux X with respect to position (R [m], Z [m]) for the double null plasma, (b) relative size and direction of displacement ξ with respect to position for the double null plasma, (c) variation in perturbed flux X with respect to position (R [m], Z [m]) forthe single null plasma, and (d) relative size and direction of displacement ξ with respect to position for the single null plasma. The perturbed flux contour passing horizontally through the magnetic axis is $X = 0$. The large number of

contours between the $X = 0$ contour and the ones passing near the X-points in (a) indicates that X is non-zero there. The small number of contours in (c) between the $X = 0$ contour and the one passing near the lower X-point indicates that X is almost zero there.

5. Perturbed flux contours for a single null TPX plasma with the closer X-point at the bottom. Contours inside and outside the plasma are shown. As required by flux conservation, the contours are continuous at the plasma surface. Kinks in the countours are indicative of surface currents.

6. The plasma separatrix, the PF coils, the passive structure, the flux loops and the gap positions for ITER. Note that gap positions 1 and 2 correspond to strike points on the divertor plates. The control coils (PF2 and PF7) are diamond-shaped for identification purposes. The $\times$'s represent flux loops.

7. The time history of the axis displacement, the perturbed current, the perturbed voltage, and the product of the last two for the PF2 control coil and the PF7 coil. These traces are based on measurements of the flux difference at the flux loop positions for the ITER configuration shown by the $\times$'s in Fig. 6.

8. The time history of the axis displacement, the perturbed current, the perturbed voltage, and the product of the last two for the PF2 control coil and the PF7 coil. These traces are based on measurements of the height of the magnetic axis ofthe ITER plasma shown in Fig. 6.

9. The time history of the perturbed currents, the perturbed voltages, and the total power of the active coils for the ITER configuration shown in Fig. 6. Also shown is the time history of the gap and axis displacements.

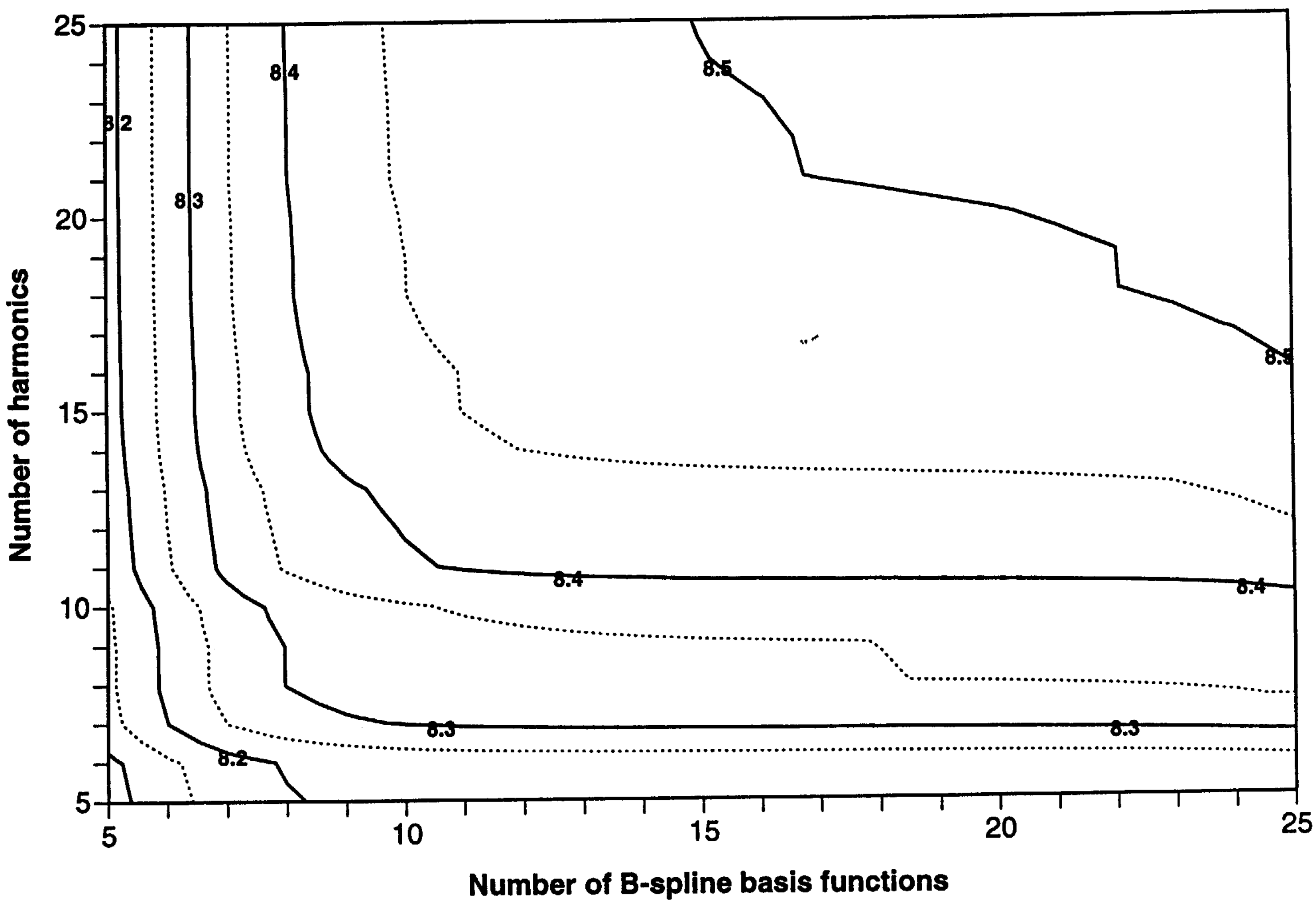

Number of harmonics
Number of B-spline basis functions
8.2
8.3
8.4
8.5
5
10
15
20
25

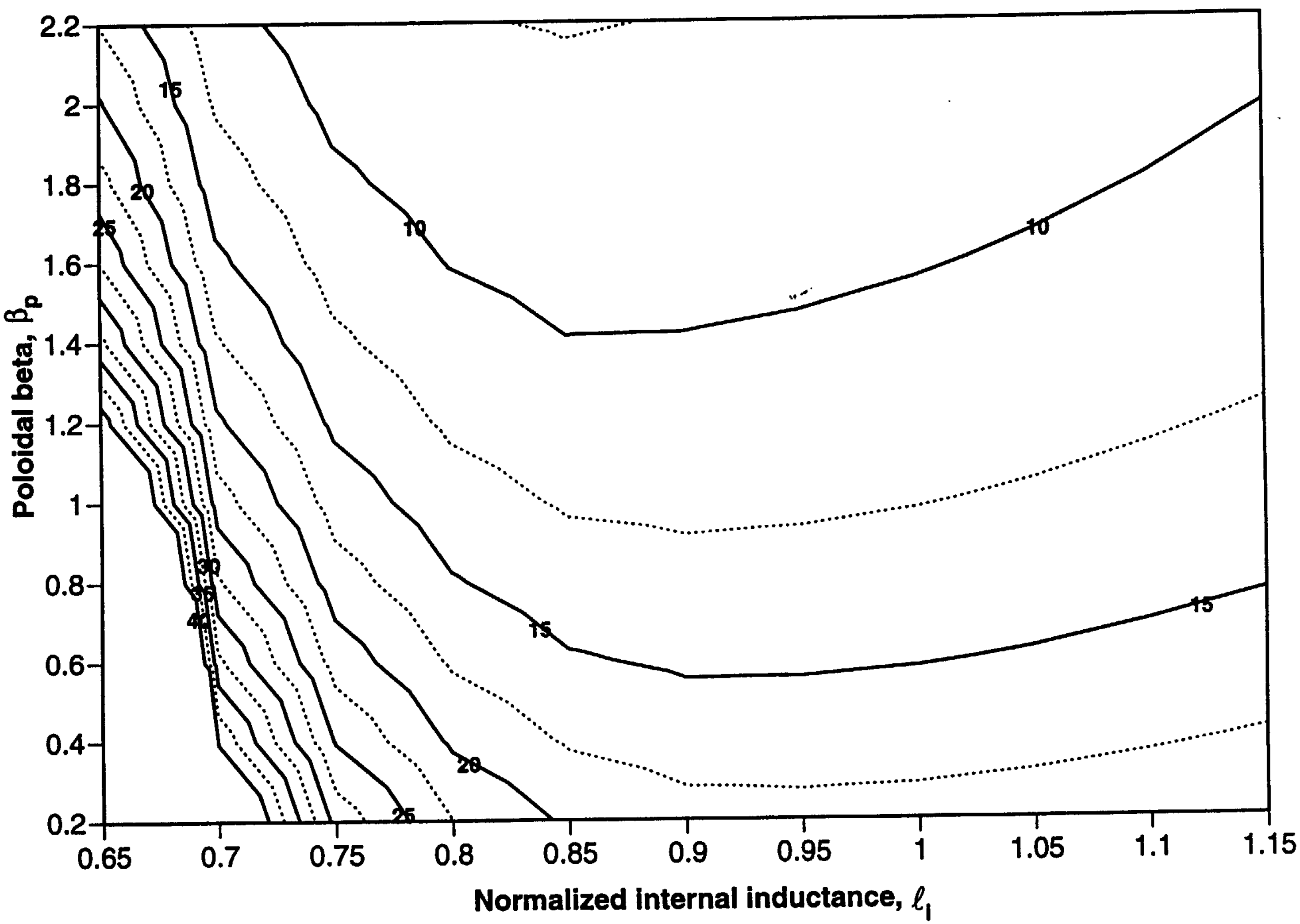

Poloidal beta, β_p
Normalized internal inductance, ℓ_i
2.2
2
1.8
1.6
1.4
1.2
1
0.8
0.6
0.4
0.2
0.65
0.7
0.75
0.8
0.85
0.9
0.95
1
1.05
1.1
1.15
10
10
15
15
15
20
20
25
25
30
35
40

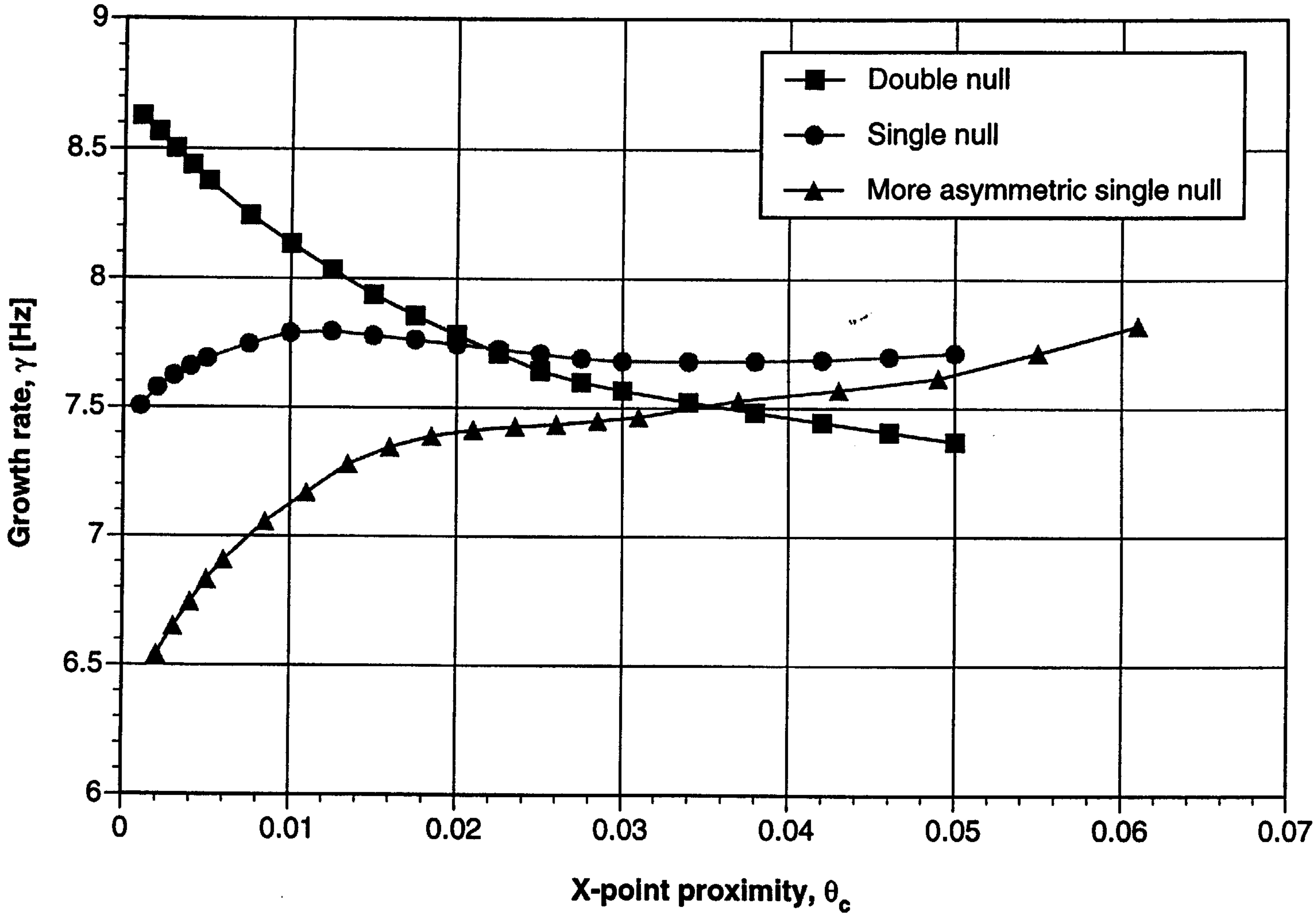

Double null
Single null
More asymmetric single null
Growth rate, γ [Hz]
X-point proximity, θ_c
9
8.5
8
7.5
7
6.5
6
0
0.01
0.02
0.03
0.04
0.05
0.06
0.07

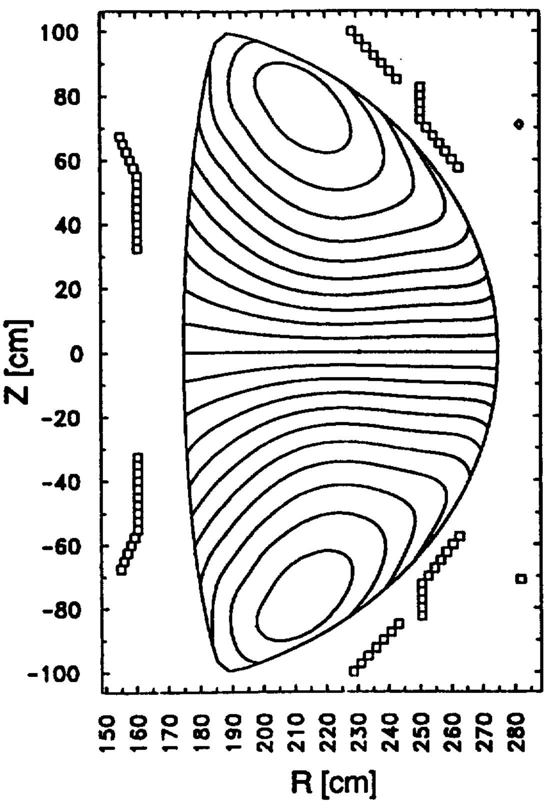

Z [cm]
100
80
60
40
20
0
-20
-40
-60
-80
-100
150 160 170 180 190 200 210 220 230 240 250 260 270 280
R [cm]

(a)

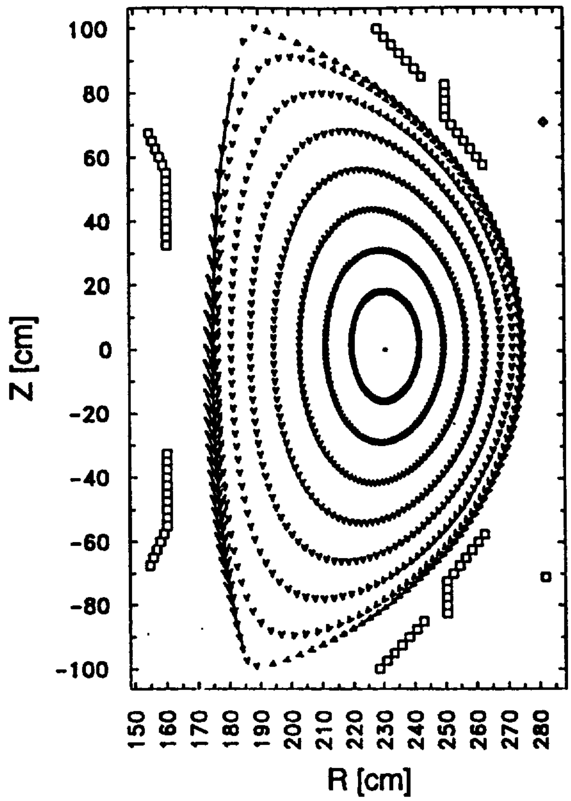

Z [cm]
100
80
60
40
20
0
-20
-40
-60
-80
-100
150 160 170 180 190 200 210 220 230 240 250 260 270 280
R [cm]

(b)

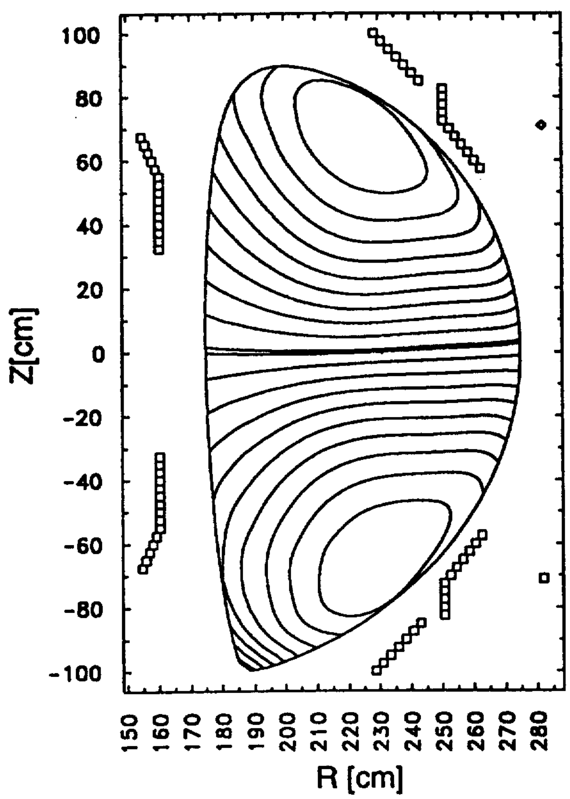

Z[cm]
100
80
60
40
20
0
-20
-40
-60
-80
-100
150 160 170 180 190 200 210 220 230 240 250 260 270 280
R [cm]

(c)

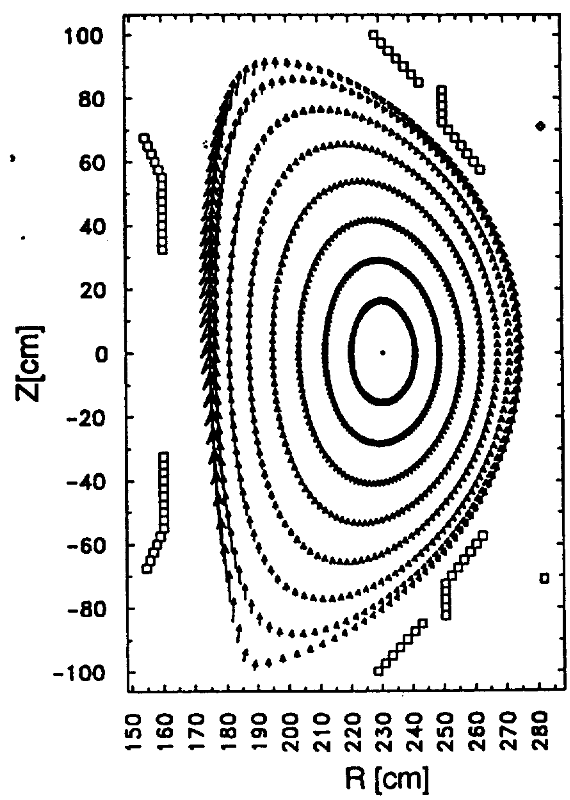

Z[cm]
100
80
60
40
20
0
-20
-40
-60
-80
-100
150 160 170 180 190 200 210 220 230 240 250 260 270 280
R [cm]

(d)

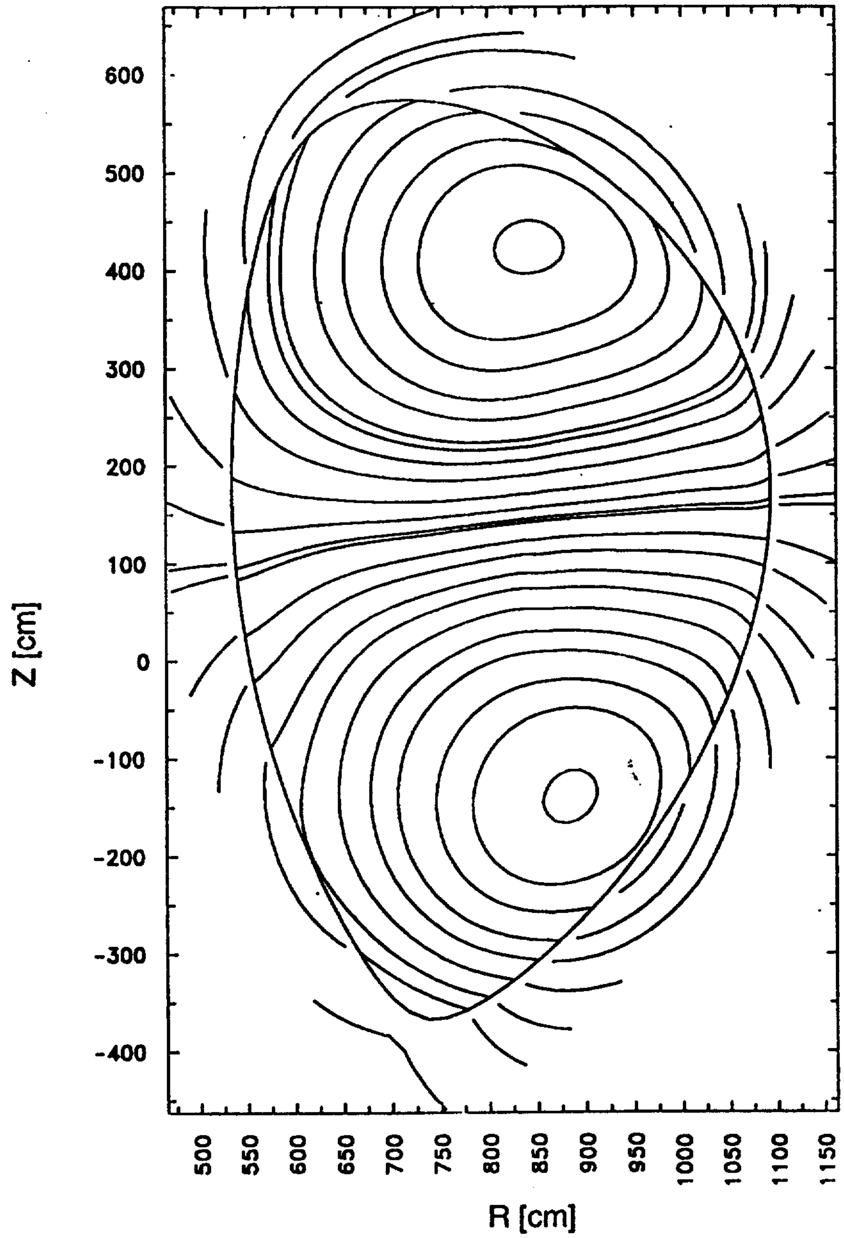

600
500
400
300
200
100
0
-100
-200
-300
-400
Z [cm]
500
550
600
650
700
750
800
850
900
950
1000
1050
1100
1150
R [cm]

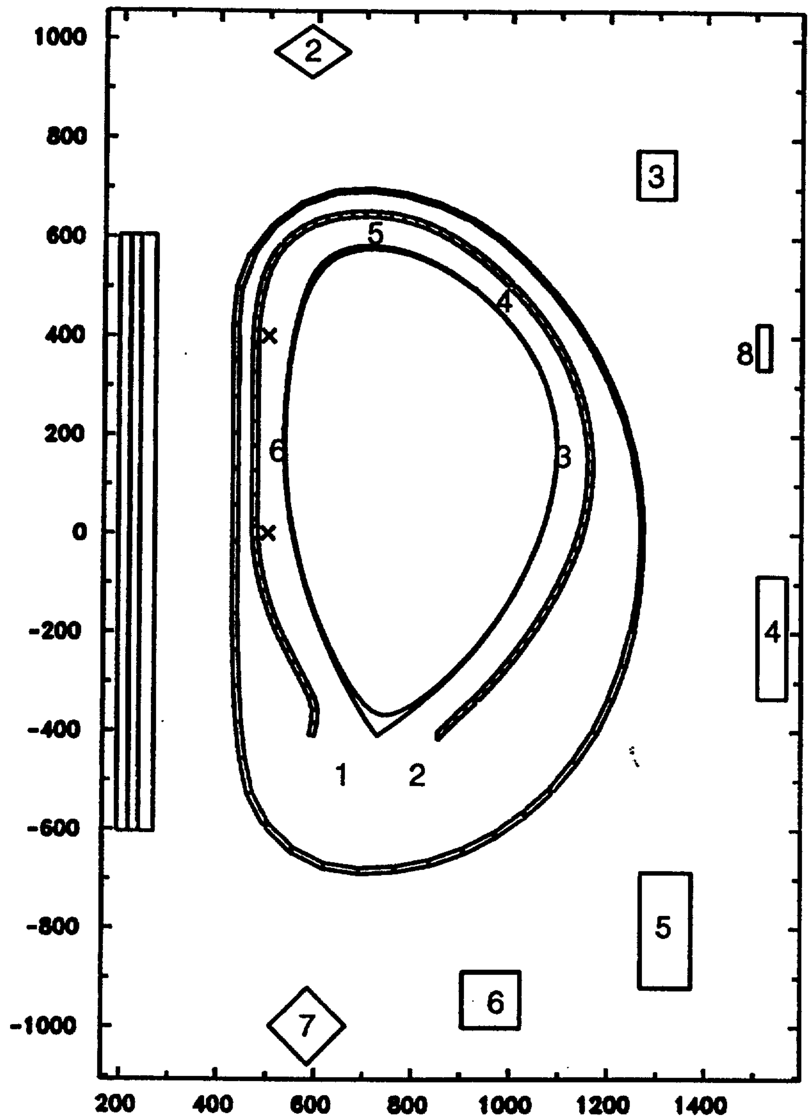

1000
800
600
400
200
0
-200
-400
-600
-800
-1000
200
400
600
800
1000
1200
1400
2
3
5
4
8
6
3
4
1
2
5
6
7

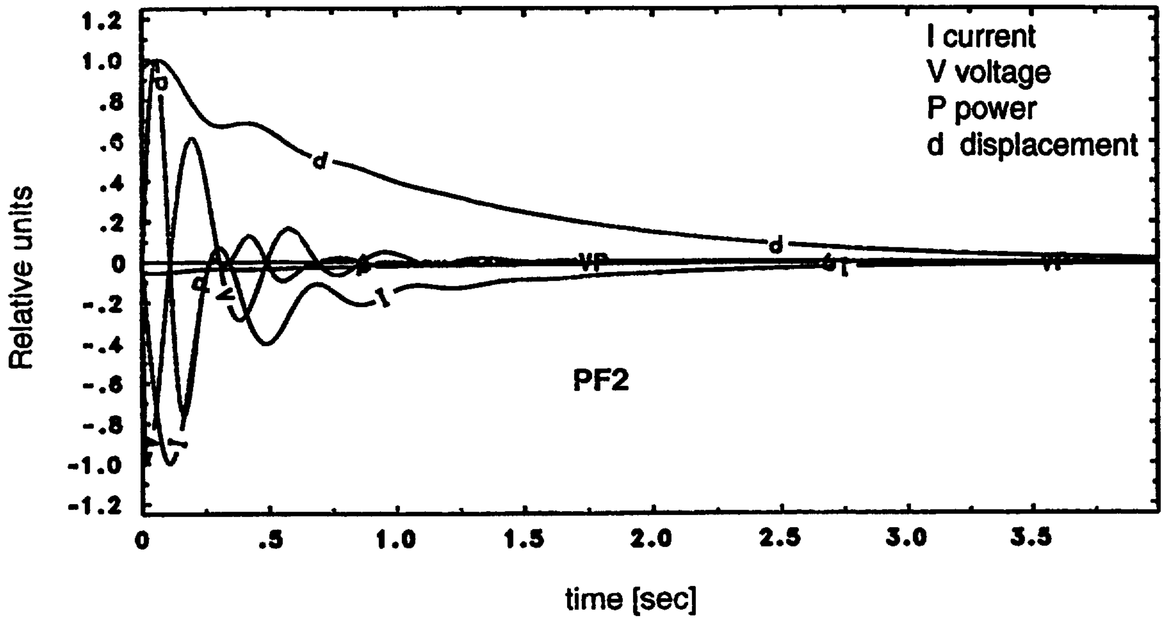

I current
V voltage
P power
d displacement
PF2
Relative units
time [sec]

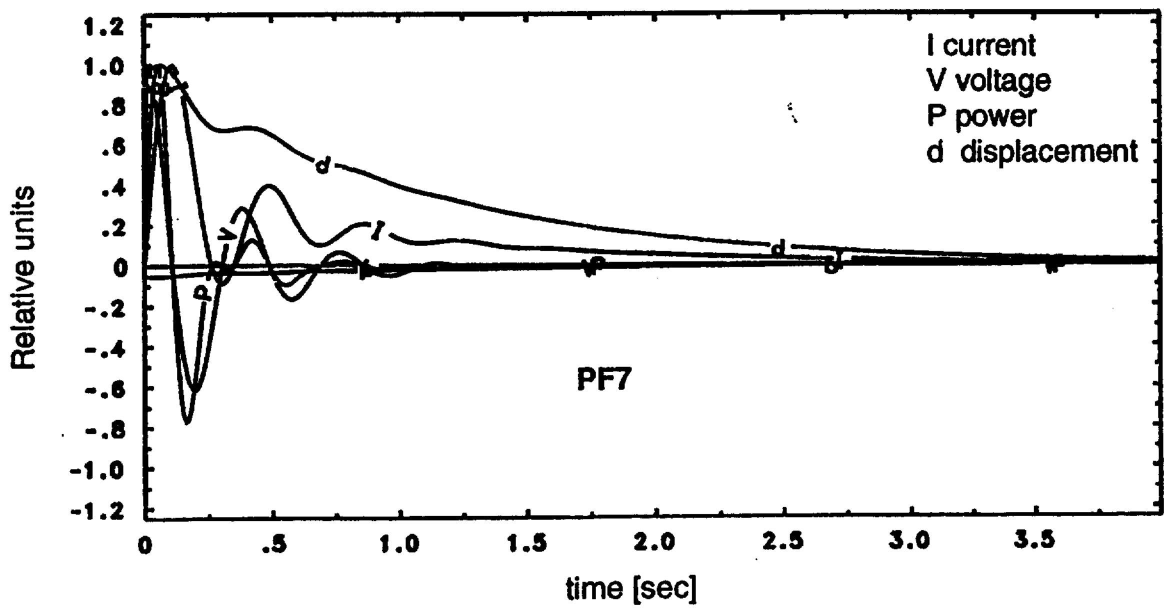

I current
V voltage
P power
d displacement
PF7
Relative units
time [sec]

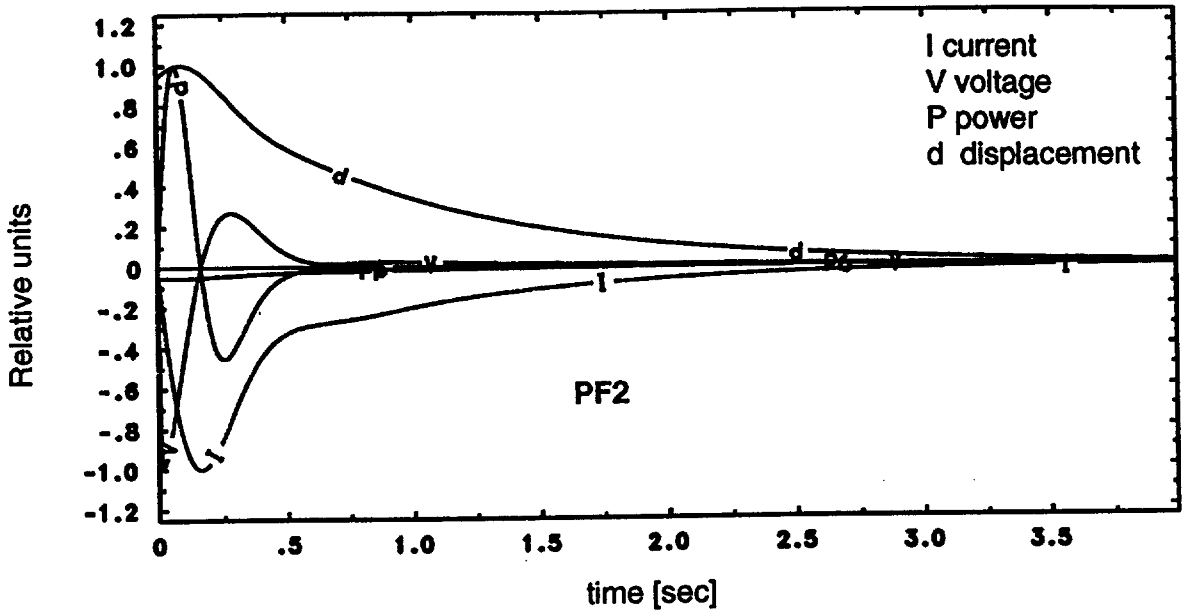
I current
V voltage
P power
d displacement
PF2
Relative units
time [sec]

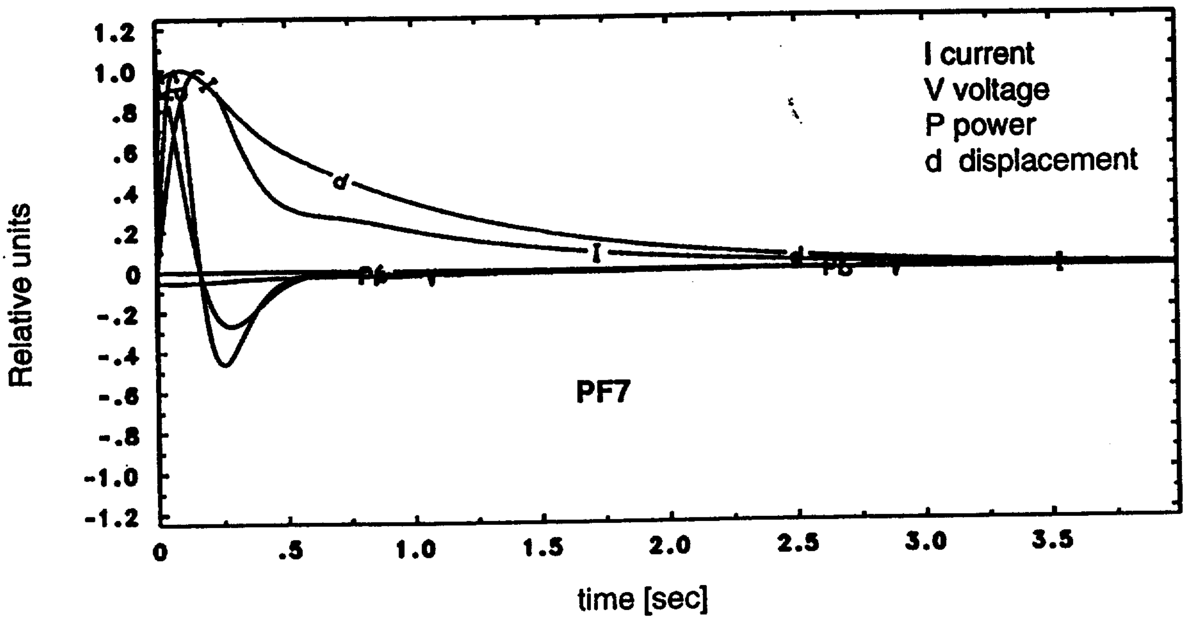
I current
V voltage
P power
d displacement
PF7
Relative units
time [sec]

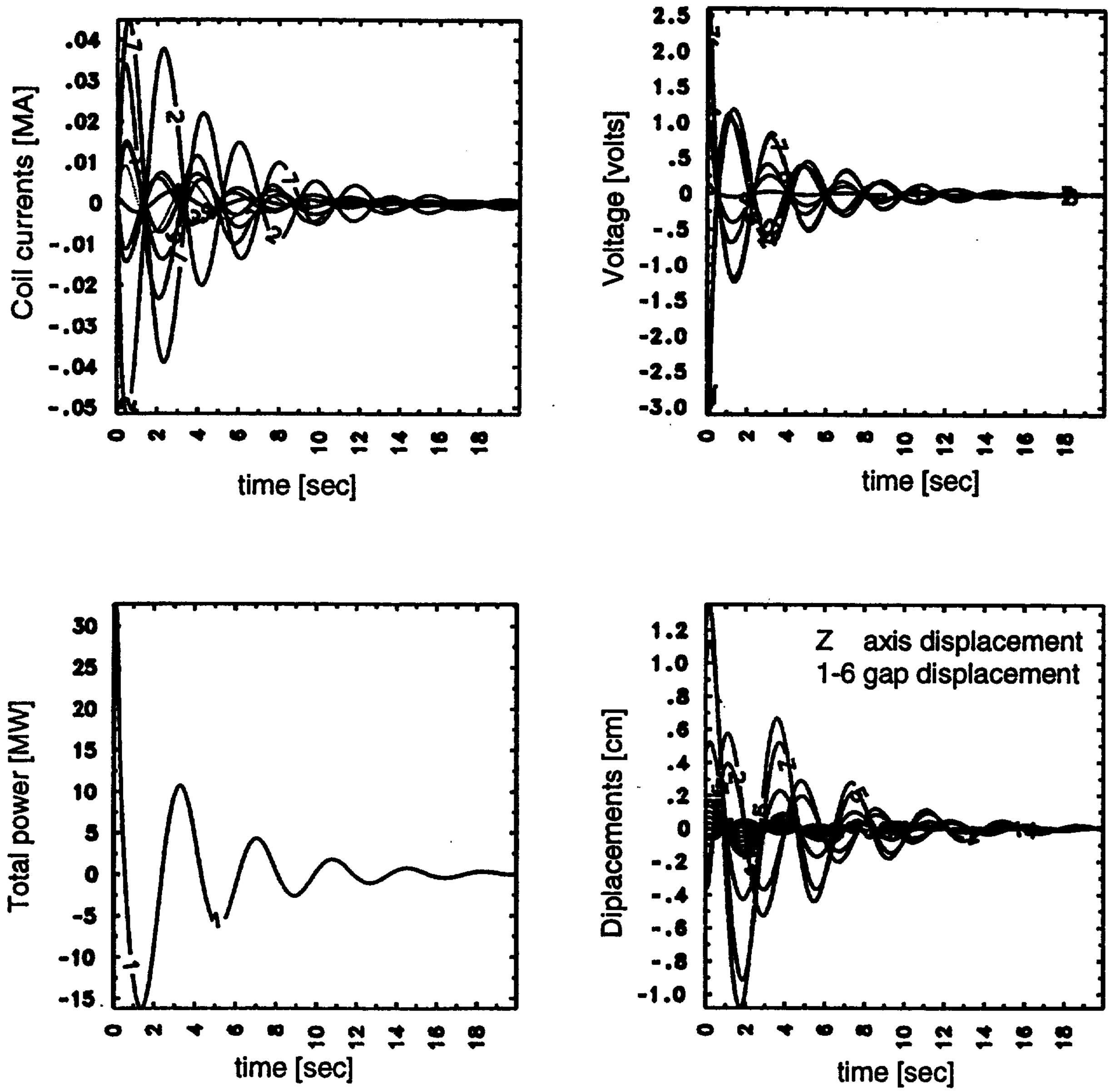

Coil currents [MA]
time [sec]
Voltage [volts]
time [sec]
Total power [MW]
time [sec]
Z axis displacement
1-6 gap displacement
Diplacements [cm]
time [sec]